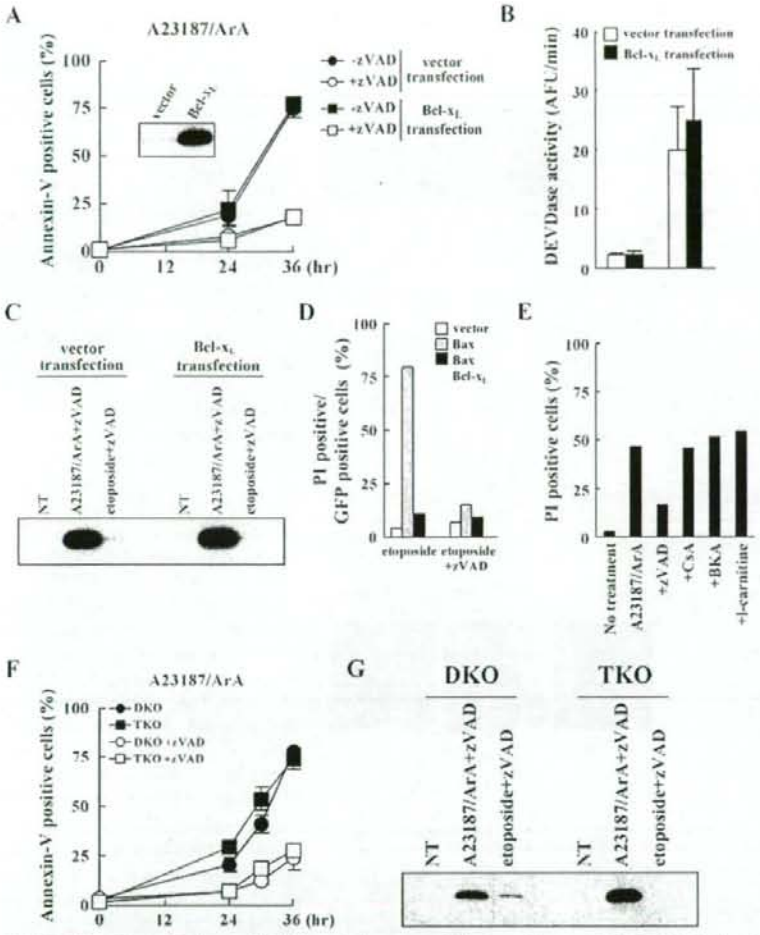

FIGURE 4. **No effect of Bcl-x_L or inhibition of the permeability transition on A23187/ArA-induced death of DKO MEFs.** *A* and *B*, overexpression of Bcl-x_L did not affect A23187/ArA-induced death of DKO MEFs. Cells were transfected with the indicated plasmids (0.5 μg). After 24 h, the cells were incubated with 10 μM A23187 plus 100 μM ArA in the presence or absence of 100 μM Z-VAD-fmk. Cell death (defined by annexin V staining) (*A*) and DEVDase activity at 24 h (*B*) were measured ($n = 4$). *C*, overexpression of Bcl-x_L did not affect A23187/ArA-induced cytochrome *c* release in DKO MEFs. DKO MEFs with or without Bcl-x_L overexpression were incubated with A23187/ArA in the presence of 100 μM Z-VAD-fmk for 18 h. Then the cytoplasmic and mitochondrial fractions were recovered, and samples were subjected to Western blotting for detection of cytochrome *c*. *NT*, not treated. *D*, Bcl-x_L inhibited Bax-induced apoptosis. DKO MEFs were transfected with plasmids expressing Bax, Bcl-x_L, or control vector together with a GFP-expressing plasmid. After 24 h, cells were treated with 100 μM etoposide in the presence or absence of 100 μM Z-VAD-fmk for another 24 h. Cell death was determined by counting the propidium iodide (*PI*)-positive cells among GFP-positive cells. *E*, mPT inhibitors failed to inhibit A23187/ArA-induced death of DKO MEFs. Cells were treated with A23187/ArA in the presence of 100 μM Z-VAD-fmk or several mPT inhibitors (1 μM CsA, 10 μM bongkrekic acid (*BKA*), or 2 mM L-carnitine). After 24 h, cell death was assessed by propidium iodide staining. *F*, lack of Cyp D did not influence A23187/ArA-induced death of DKO MEFs. DKO MEFs (Bax/Bak-deficient) and TKO MEFs (Bax/Bak/Cyp D-deficient) were incubated with A23187/ArA in the presence or absence of 100 μM Z-VAD-fmk. Then cell death was assessed by annexin V staining ($n = 4$). *G*, lack of Cyp D did not affect A23187/ArA-induced cytochrome *c* release. The same experiment as in *C* was performed, except for the use of TKO MEFs and DKO MEFs.

undergo caspase-independent death (data not shown). These results indicated that A23187/ArA induced caspase-dependent death of immortalized MEFs in both a Bax/Bak-dependent and a Bax/Bak-independent manner.

To examine whether mitochondria were involved in the A23187/ArA-induced caspase-dependent death of DKO MEFs, we used gene silencing with siRNA to down-regulate caspase-9 and cytochrome *c*. Caspase-9 is activated by forming a complex called the apoptosome with Apaf-1 and cytochrome *c* in the presence of (d)ATP (9). Proteolytic activation of caspase-9 leads to activation of caspase-3 (9). Endogenous caspase-9 and cytochrome *c* were silenced in DKO MEFs by the respective siRNAs (Fig. 2, *A* and *C*). Silencing of caspase-9 and cytochrome *c* in DKO MEFs markedly reduced A23187/ArA-induced death, as assessed by annexin V staining, but did not completely abolish it (Fig. 2, *B* and *D*). Although silencing of caspase-9 only partially inhibited the activation of DEVDase (Fig. 2*B*), probably due to incomplete silencing (Fig. 2*A*), silencing of cytochrome *c* inhibited more strongly the activation of DEVDase (Fig. 2*D*). These results indicated that A23187/ArA-induced caspase activation required the presence of Apaf-1/cytochrome *c*. Incomplete inhibition of cell death after silencing of cytochrome *c* was mainly due to the simultaneous occurrence of caspase-independent death because the addition of Z-VAD-fmk did not further reduce A23187/ArA-induced death, as shown in Fig. 2*D*. To avoid the influence of mitochondrial respiration in the experiment with silencing of cytochrome *c*, we also performed the experiment in the presence of antimycin A (an inhibitor of respiration) and, although antimycin A enhanced cell death, virtually identical results were obtained (Fig. 2*E*). These results indicated that A23187/ArA-induced caspase-dependent death required the presence of Apaf-1/caspase-9/cytochrome *c* but not Bax/Bak.

We next examined whether cytochrome *c* was released from the mitochondria in A23187/ArA-treated DKO MEFs. Subcellular fractionation revealed that etoposide induced cytochrome *c* release in WT MEFs but not DKO MEFs (data not shown), whereas A23187/ArA caused cytochrome *c* release from both

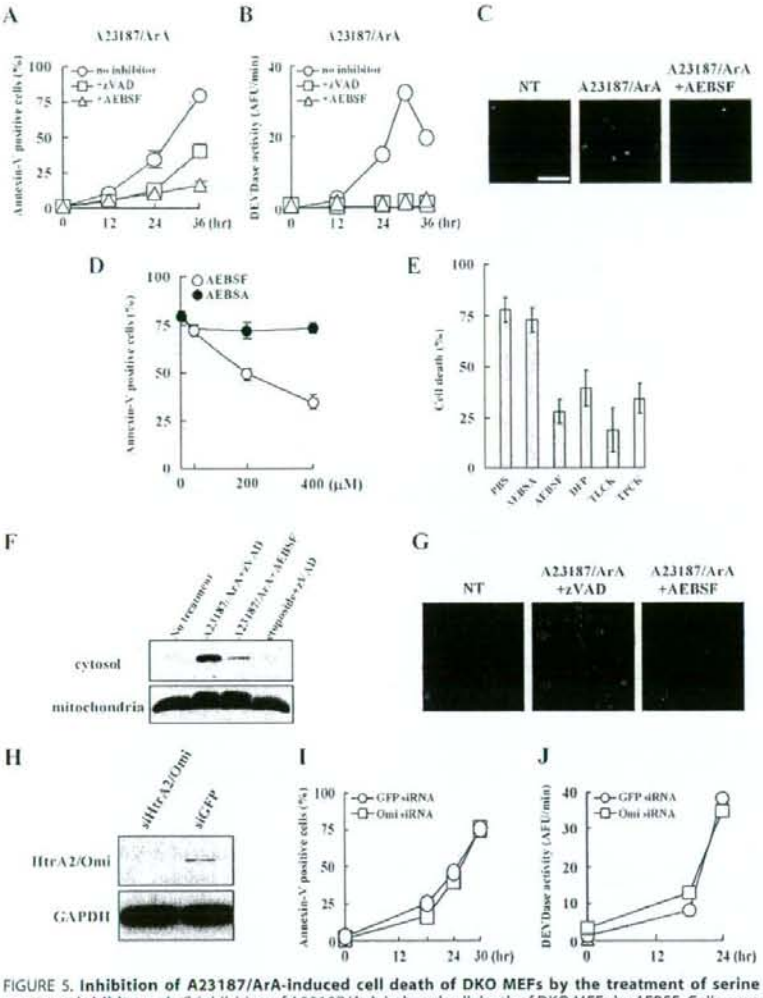

FIGURE 5. **Inhibition of A23187/ArA-induced cell death of DKO MEFs by the treatment of serine protease inhibitors.** *A–C*, inhibition of A23187/ArA-induced cell death of DKO MEFs by AEBSF. Cells were incubated with 10 μM A23187 plus 100 μM ArA in the presence or absence of 100 μM Z-VAD-fmk or 100 μg/ml AEBSF. Then cell death (defined by annexin V staining) (*A*) and DEVDase activity (*B*) were measured ($n = 4$). Representative nuclear morphology of A23187/ArA-treated DKO MEFs in the presence or absence of AEBSF at 24 h is shown in *C*. *NT*, not treated. *Bars*, 50 μm. *D*, inhibition of A23187/ArA-induced cell death by AEBSF but not AEBSA, an inactive analog. DKO MEFs were incubated with A23187/ArA in the presence of 40, 200, and 400 μM AEBSF or AEBSA. After 30 h, the extent of cell death was assessed by annexin V staining. Data are shown as the mean ± S.D. ($n = 3$). *E*, inhibition of A23187/ArA-induced cell death by various serine protease inhibitors. Serine protease inhibitors, AEBSF, DFP, TLCK, and TPCK or the negative control (AEBSA and PBS) were microinjected into the DKO MEFs with GFP as described under "Experimental Procedures." After 1 h, cells were treated with A23187/ArA, and the cell death was assessed after 20 h. Cell viability was determined by counting GFP-positive cells attached on the dish among total injected GFP-positive cells. Data are shown as the mean ± S.D. ($n = 3$). *F* and *G*, inhibition of A23187/ArA-induced cytochrome *c* release by AEBSF. DKO MEFs were not treated or were treated with A23187/ArA in the presence of Z-VAD-fmk (100 μM) or AEBSF (100 μg/ml) for 18 (*F*) or 12 h (*G*). In *F*, the cytoplasmic fraction was recovered, and samples were subjected to Western blotting for detection of cytochrome *c*. In *G*, MEFs were fixed and immunostained with an anti-cytochrome *c* monoclonal antibody. *H–J*, no inhibition of A23187/ArA-induced cell death by silencing of HtrA2/Omi, a mitochondrial serine protease, was shown. *H*, DKO MEFs were treated with 10 μg of HtrA2/Omi siRNA as described under "Experimental Procedures," after which the expression of HtrA2/Omi and GAPDH (loading control) was analyzed by Western blotting. DKO MEFs with silencing of HtrA2/Omi or GFP (control) were treated with A23187/ArA, after which cell death (defined by annexin-V staining) (*I*) and DEVDase activity (*J*) were measured ($n = 4$).

WT and DKO MEFs in the presence of Z-VAD-fmk (Fig. 3*A*). Consistent with this result, cytochrome *c* localization was altered in A23187/ArA-treated DKO MEFs, but not etoposide-treated DKO MEFs, as assessed by immunofluorescence microscopy (Fig. 3*B*). All these findings indicated that A23187/ArA induced cytochrome *c* release in a Bax/Bak-independent manner and subsequently activated caspases to induce cell death.

How was cytochrome *c* released from the mitochondria in a Bax/Bak-independent manner after treatment with A23187/ArA? First, we examined whether Bcl-x_L could inhibit this Bax/Bak-independent process of cytochrome *c* release. As shown in Fig. 4*A*, a pan-caspase inhibitor, but not overexpression of Bcl-x_L, inhibited A23187/ArA-induced death of DKO MEFs. Consistent with this result, activation of both caspases and cytochrome *c* release was not influenced by Bcl-x_L (Fig. 4, *B* and *C*). As expected, the expression of Bcl-x_L markedly inhibited etoposide-induced apoptosis in Bax-transfected DKO MEFs (Fig. 4*D*).

ArA and Ca^{2+} ionophore A23187 are thought to induce the mPT (8, 10, 11), which is a Ca^{2+}-dependent, cyclosporin A (CsA)-sensitive increase of mitochondrial membrane permeability that allows various solutes to equilibrate across the membranes (12). Since the CsA-sensitive mPT has been suggested to have a role in apoptotic cytochrome *c* release, we investigated whether it was also involved in A23187/ArA-induced Bax/Bak-independent cytochrome *c* release and cell death. Accordingly, CsA, bongkrekic acid, and L-carnitine, all of which are known to inhibit the mPT (12, 13), were added to cultures of A23187/ArA-treated DKO MEFs. As shown in Fig. 4*E*, none of these reagents inhibited A23187/ArA-induced death, whereas Z-VAD-fmk caused significant inhibition, suggesting that the mPT was not involved in this mode of cell death. To confirm this possibility,

we employed mice lacking cyclophilin D (Cyp D), in which the CsA-sensitive mPT is completely blocked (14). Cross-breeding produced $Bax^{-/-}Bak^{-/-}$Cyp $D^{-/-}$ (TKO) mice, from which immortalized MEFs were obtained. As shown in Fig. 4*F*, A23187/ArA equally induced the death of TKO and DKO MEFs, with cell death being partially inhibited by Z-VAD-fmk. Consistent with these findings, cytochrome *c* release was also observed in A23187/ArA-treated TKO MEFs (Fig. 4*G*), indicating that the CsA-sensitive mPT was not involved in Bax/Bak-independent cytochrome *c* release and cell death induced by A23187/ArA.

To obtain some insight into the molecular mechanisms of A23187/ArA-induced cytochrome *c* release, we tested the effects of various drugs, such as protease inhibitors and lipase inhibitors, on A23187/ArA-treated DKO MEFs and found that AEBSF, which inhibits serine proteases through sulfonylation of the active site serine residue (15) and has been described to inhibit some forms of cell death (16–19), could prevent A23187/ArA-induced caspase activation and cell death (Fig. 5, *A–C*). AEBSF inhibited A23187/ArA-induced cell death in a dose-dependent manner, whereas AEBSA, an inactive analog of AEBSF, did not inhibit it at any doses tested (Fig. 5*D*). To confirm the involvement of a serine protease(s), we examined other serine protease inhibitors, DFP, TLCK, and TPCK. The addition of DFP, TLCK, and TPCK into culture medium did not inhibit A23187/ArA-induced death (data not shown), which could be due to their membrane impermeability; therefore, we microinjected them into cells. As shown in Fig. 5*E*, all the serine protease inhibitors inhibited A23187/ArA-induced cell death. Since inhibitors are diluted to 2.5×10^2-10^3-fold in the cytoplasm (20), the estimated intracellular concentrations of AEBSF are calculated to 40–400 nM. AEBSF not only inhibited A23187/ArA-induced cell death but also blocked cytochrome *c* release (Fig. 5, *F* and *G*). These results indicated that a serine protease(s) is involved in the process of A23187/ArA-induced cell death upstream of cytochrome *c* release. AEBSF was a more effective inhibitor of A23187/ArA-induced cell death than Z-VAD-fmk (Fig. 5*A*), suggesting that it acted at a common step further upstream in the death-signaling pathways or that it inhibited independently both caspase-dependent and caspase-independent cell death. We examined the influence of HtrA2/Omi, a serine protease located in the mitochondria that is known to be involved in apoptosis (21, 22). As shown in Fig. 5, *H–J*, silencing of HtrA2/Omi had no effect on A23187/ArA-induced death, although it significantly reduced Fas-mediated apoptosis of DKO MEFs (data not shown).

DISCUSSION

This study revealed the following findings. 1) the combination of Ca^{2+} ionophore A23187 and arachidonic acid causes caspase-dependent cell death following cytochrome *c* release as well as caspase-independent death in Bax/Bak double-knock-out MEFs. 2) The Bcl-2 family of proteins and the CsA-sensitive mPT are not involved in this mode of cell death. 3) Instead, this mode of death is mediated by an unknown serine protease(s). These findings demonstrate the existence of a novel mechanism of cytochrome *c* release that is regulated by serine proteases but not by the Bcl-2 family.

Bax/Bak-dependent and Bax/Bak-independent mechanisms seem to respond to different stimuli. After treatment with etoposide, UV, or staurosporine, cytochrome *c* release occurred in a Bcl-2 family-dependent manner, whereas A23187/ArA not only induced cytochrome *c* release in a Bcl-2 family-dependent manner but also in a Bcl-2 family-independent, serine protease(s)-dependent manner. This difference might be related to the influence of molecule(s) acting upstream of the mitochondria. Since apoptosis induced by BH3-only proteins occurs in a Bax/Bak-dependent manner (23, 24), A23187/ArA probably activates unidentified apoptotic molecule(s) in addition to BH3-only proteins. A23187/ArA interferes with intracellular Ca^{2+} homeostasis (5), so Ca^{2+} itself or Ca^{2+}-regulated proteins might be involved in the mechanism of A23187/ArA-induced cell death. If the Ca^{2+} ion was a major signal mediator, it seemed likely that cytochrome *c* release would occur via mPT. However, we excluded this possibility by employing MEFs deficient in Bax, Bak, and Cyp D (Fig. 4, *F* and *G*). This result was consistent with our findings obtained in Cyp $D^{-/-}$ MEFs and mice (14) that cell death mediated via the mPT is necrosis but not apoptosis, probably due to the decline of ATP caused by $\Delta\psi$ loss. Therefore, a Ca^{2+}-regulated protein, rather than Ca^{2+} itself, may be the most suitable candidate as an inducer of Bax/Bak-independent cytochrome *c* release. We could not formally exclude the possibility that A23187/ArA-induced cytochrome *c* release was mediated by the CsA-insensitive mPT.

Since A23187/ArA-induced death of DKO MEFs was inhibited by the treatment of serine protease inhibitors including AEBSF and TPCK, proteolytic activity of a serine protease(s) seems to be involved in this form of cell death. Although it is still to be determined how serine protease inhibitors suppressed A23187/ArA-induced death, the possibility was excluded that AEBSF inhibited A23187/ArA-induced death by blocking mitochondrial Ca^{2+} uptake, by using Rhod2-AM as an indicator of mitochondrial Ca^{2+} uptake.[3] A serine protease(s) may cleave one or more unidentified substrates in the mitochondria that are involved in the regulation of death due to A23187/ArA. For example, a mitochondrial channel protein might be cleaved by a serine protease(s), resulting in conformational changes that allow cytochrome *c* release, but elucidation of the actual mechanism will require further investigation.

A serine protease(s)-mediated, but not Bax/Bak-mediated, cytochrome *c* release and caspase-dependent cell death were observed in immortalized MEFs. Do other normal cells also have the potential to undergo these forms of death? It has previously been described that the brains of $bax^{-/-}bak^{-/-}$ mice displayed a normal gross anatomy, regardless of the fact that neuronal progenitor cells derived from these mice are strongly resistant to apoptosis (25, 26). Note that mature neurons present in cerebellar granule cell cultures from $bax^{-/-}bak^{-/-}$ mice are as sensitive to excitotoxic cell death

[3] T. Mizuta, S. Shimizu, and Y. Tsujimoto, unpublished results.

as wild type cells (26). The excitotoxic cell death has both necrotic as well as apoptotic features (27), and some excitotoxins induce nitric oxide production, which can cause cell death with apoptotic features (28). In excitotoxic death of cerebellar granule cells, novel apoptotic mechanisms, which are Bax/Bak-independent, might be activated.

In conclusion, we demonstrated the existence of a novel mechanism of cytochrome *c* release that involves a serine protease(s) but not the mPT or Bcl-2 family proteins.

REFERENCES

1. Wang, X. (2001) *Genes Dev.* **15,** 2922–2933
2. Wolf, B. B., and Green, D. R. (2002) *Curr. Biol.* **12,** R177–R179
3. Tsujimoto, Y. (2003) *J. Cell. Physiol.* **195,** 158–167
4. Wei, M. C., Zong, W. X., Cheng, E. H., Lindsten, T., Panoutsakopoulou, V., Ross, A. J., Roth, K. A., MacGregor, G. R., Thompson, C. B., and Korsmeyer, S. J. (2001) *Science* **292,** 727–730
5. Scorrano, L., Oakes, S. A., Opferman, J. T., Cheng, E. H., Sorcinelli, M. D., Pozzan, T., and Korsmeyer, S. J. (2003) *Science* **300,** 135–139
6. Hakem, R., Hakem, A., Duncan, G. S., Henderson, J. T., Woo, M., Soengas, M. S., Elia, A., de la Pompa, J. L., Kagi, D., Khoo, W., Potter, J., Yoshida, R., Kaufman, S. A., Lowe, S. W., Penninger, J. M., and Mak, T. W. (1998) *Cell* **94,** 339–352
7. Pompeia, C., Lima, T., and Curi, R. (2003) *Cell Biochem. Funct.* **21,** 97–104
8. Orrenius, S., Zhivotovsky, B., and Nicotera, P. (2003) *Nat. Rev. Mol. Cell Biol.* **4,** 552–565
9. Li, P., Nijhawan, D., Budihardjo, I., Srinivasula, S. M., Ahmad, M., Alnemri, E. S., and Wang, X. (1997) *Cell* **91,** 479–489
10. Petronilli, V., Penzo, D., Scorrano, L., Bernardi, P., and Di Lisa, F. (2001) *J. Biol. Chem.* **276,** 12030–12034
11. Scorrano, L., Penzo, D., Petronilli, V., Pagano, F., and Bernardi, P. (2001) *J. Biol. Chem.* **276,** 12035–12040
12. Halestrap, A. P., McStay, G. P., and Clarke, S. J. (2002) *Biochimie (Paris)* **84,** 153–166
13. Di Lisa, F., Bobyleva-Guarriero, V., Jocelyn, P., Toninello, A., and Siliprandi, N. (1985) *Biochem. Biophys. Res. Commun.* **131,** 968–973
14. Nakagawa, T., Shimizu, S., Watanabe, T., Yamaguchi, O., Otsu, K., Yamagata, H., Inohara, H., Kubo, T., and Tsujimoto, Y. (2005) *Nature* **434,** 652–658
15. Markwardt, F., Drawert, J., and Walsmann, P. (1974) *Biochem. Pharmacol.* **23,** 2247–2256
16. Kagaya, S., Kitanaka, C., Noguchi, K., Mochizuki, T., Sugiyama, A., Asai, A., Yasuhara, N., Eguchi, Y., Tsujimoto, Y., and Kuchino, Y. (1997) *Mol. Cell. Biol.* **17,** 6736–6745
17. de Bruin, E. C., Meersma, D., de Wilde, J., den Otter, I., Schipper, E. M., Medema, J. P., and Peltenburg, L. T. (2003) *Cell Death Differ.* **10,** 1204–1212
18. Egger, L., Schneider, J., Rheme, C., Tapernoux, M., Hacki, J., and Borner, C. (2003) *Cell Death Differ.* **10,** 1188–1203
19. Rideout, H. J., Zang, E., Yeasmin, M., Gordon, R., Jabado, O., Park, D. S., and Stefanis, L. (2001) *Neuroscience* **107,** 339–352
20. Matsuoka, Y., Takechi, S., Nakayama, T., and Yoneda, Y. (1994) *J. Cell Sci.* **107,** 693–701
21. Suzuki, Y., Imai, Y., Nakayama, H., Takahashi, K., Takio, K., and Takahashi, R. (2001) *Mol. Cell* **8,** 613–621
22. Hegde, R., Srinivasula, S. M., Zhang, Z., Wassell, R., Mukattash, R., Cilenti, L., DuBois, G., Lazebnik, Y., Zervos, A. S., Fernandes-Alnemri, T., and Alnemri, E. S. (2002) *J. Biol. Chem.* **277,** 432–438
23. Cheng, E. H., Wei, M. C., Weiler, S., Flavell, R. A., Mak, T. W., Lindsten, T., and Korsmeyer, S. J. (2001) *Mol. Cell* **8,** 705–711
24. Zong, W. X., Lindsten, T., Ross, A. J., MacGregor, G. R., and Thompson, C. B. (2001) *Genes Dev.* **15,** 1481–1486
25. Lindsten, T., Ross, A. J., King, A., Zong, W. X., Rathmell, J. C., Shiels, H. A., Ulrich, E., Waymire, K. G., Mahar, P., Frauwirth, K., Chen, Y., Wei, M., Eng, V. M., Adelman, D. M., Simon, M. C., Ma, A., Golden, J. A., Evan, G., Korsmeyer, S. J., MacGregor, G. R., and Thompson, C. B. (2000) *Mol. Cell* **6,** 1389–1399
26. Lindsten, T., Golden, J. A., Zong, W. X., Minarcik, J., Harris, M. H., and Thompson, C. B. (2003) *J Neurosci.* **23,** 11112–11119
27. Ankarcrona, M., Dypbukt, J. M., Bonfoco, E., Zhivotovsky, B., Orrenius, S., Lipton, S. A., and Nicotera, P. (1995) *Neuron* **15,** 961–973
28. Brune, B. (2003) *Cell Death Differ.* **10,** 864–869

WILEY InterScience®
PROTEINS
STRUCTURE • FUNCTION • BIOINFORMATICS

STRUCTURE NOTE

Crystal structure of human cyclophilin D in complex with its inhibitor, cyclosporin A at 0.96-Å resolution

Kenji Kajitani,[1] Masahiro Fujihashi,[1] Yukiko Kobayashi,[1] Shigeomi Shimizu,[2] Yoshihide Tsujimoto,[2] and Kunio Miki[1]*

[1] Department of Chemistry, Graduate School of Science, Kyoto University, Sakyo-Ku, Kyoto 606-8502, Japan

[2] Laboratory of Molecular Genetics, Department of Medical Genetics, Osaka University Medical School and SORST of JST, Suita, Osaka 565-0871, Japan

Key words: CypD; PPIase (peptidyl-prolyl cis-trans isomerase); CsA; complex preparation; crystal structure.

INTRODUCTION

Cyclophilins belong to a ubiquitous protein family that catalyses the reaction of peptidyl-prolyl *cis-trans* isomerase (PPIase) on their ligand proteins, and they play a crucial role in protein folding.[1–3] Proteins in the cyclophilin family are found in a variety of organisms from prokaryotes to eukaryotes, including humans.[4] Five isoforms are known among human cyclophlins.[2,5,6] One of these isoforms, cyclophilin D (CypD), is a mitochondria-specific cyclophilin.[2] CypD is known to play a pivotal role in mitochondrial permeability transition (MPT), which leads to the loss of mitochondrial membrane potential ($\Delta\Psi$), mitochondrial swelling, rupture of the outer membrane, and finally necrotic cell death.[7] CypD knock-out mice do not have any detectable phenotypic anomalies, but they resist ischemia/reperfusion-induced injury in the heart[8,9] and brain.[10] Although the exact target protein molecule for CypD PPIase activity is still unknown, these findings reported to date have suggested CypD as a potential drug target to treat cerebral and myocardial infarctions.

An immunosuppressive compound, cyclosporin A (CsA), is known to bind to the proteins of this family and inhibits PPIase activity of cyclophilins and MPT.[3,11] Several crystal structures of cyclophilin including that of CypD have been determined,[12–14] but thus far, no structures of CypD complexed with ligands have been determined. It is essential to obtain structural information about CypD-ligand interactions for the development of a CypD-specific inhibitor as an anti-infarction drug. Accordingly, we have determined the ultrahigh resolution crystal structure of CypD in complex with CsA at 0.96-Å resolution.

MATERIALS AND METHODS

The human CypD expression system starting from Gly2 was constructed as described by Schlatter *et al.*[14] The calculated molecular weight of this CypD recombinant is 17.8 kDa. The gene was cloned into a pET-21a vector (NOVAGEN) using the NdeI and BamHI restriction sites, and a mutation of Lys133 into Ile was introduced on the CypD gene. Expression was conducted in *Escherichia coli* BL21(DE3) cells. Cell culturing and the induction of CypD expression were also performed as previously described.[14] Purification was performed with Hi-trap SP, RESOURCE Q, and Superdex 75 chromatography instead of with the EMD COO^-, Q-sepharose, and EMD BioSEC columns used by Schlatter *et al.*[14] The

Grant sponsor: Ministry of Education, Culture, Sports, Science and Technology of Japan (National Project on Protein Structural and Functional Analyses).
Shigeomi Shimizu's current address is Department of Pathological Cell Biology, Medical Research Institute, Tokyo Medical and Dental University, Bunkyo-Ku, Tokyo 113-8510.
*Correspondence to: Kunio Miki, Department of Chemistry, Graduate School of Science, Kyoto University, Sakyo-ku, Kyoto 606-8502, Japan.
E-mail: miki@kuchem.kyoto-u.ac.jp
Received 9 August 2007; Revised 30 September 2007; Accepted 2 October 2007
Published online 12 December 2007 in Wiley InterScience (www.interscience.wiley.com). DOI: 10.1002/prot.21855

supernatant of the cell homogenate was applied to a Hi-trap SP column equilibrated with buffer A (100 m*M* Tris-HCl at pH 7.8, 2 m*M* EDTA, and 2 m*M* DTT). Bound CypD proteins were eluted with a gradient of 0–0.5 *M* NaCl. The CypD fractions were desalted with dialysis against buffer A and applied onto a ResourceQ column equilibrated with buffer A. CypD did not bind to the column, and the flowthrough fraction was further purified with a Superdex75 column equilibrated with buffer B (50 m*M* potassium phosphate at pH 7.3, 100 m*M* NaCl, 2 m*M* EDTA, and 2 m*M* DTT). Thirteen milligrams of CypD were harvested from 5 g of *E. coli* cells.

For the crystallization, 25 mg/mL of purified CypD in buffer B was used. CsA, isolated from the fungus *Tolypocladium inflatum*, was purchased from CALBIOCHEM. Two milligrams of CsA powder were incubated with 100 μL of CypD solution for 5 days in order to obtain the CypD and CsA complex. The nondissolved CsA was removed with a 0.22-μm filter. Rod-shaped crystals of the complex were obtained within a day using 20% polyethylene glycol 3350, 45 m*M* sodium-citrate buffer at pH 2.9 as a precipitant solution. The crystals were grown to an approximate maximum rod-length of 1.0 mm.

The crystals were dipped in a cryoprotectant buffer (35% polyethylene glycol 3350, sodium-citrate buffer at pH 2.9) for ~10 s and were flash-frozen in a nitrogen gas stream at 100 K. Two sets of diffraction data were collected at the beamline NW12A at Photon Factory, Ibaraki, and at the beamline BL41XU at SPring-8, Hyogo, Japan. The initial dataset was collected with a wavelength of 1.000 Å in Photon Factory. The crystal was exposed for 1.0 s for 1.0° oscillation with a 0.5-mm aluminum attenuator for the low-resolution dataset, and for 3.0 s for 0.5° oscillation without the aluminum attenuator for the high-resolution dataset. The images were integrated with HKL2000[15] from 50 to 2.2 Å and from 2.5- to 1.06-Å resolution for the low- and high-resolution datasets, respectively. The merged data were phased with the molecular replacement method using Molrep.[16,17] The structure of human apo-CypD (PDB ID: 2BIT) was employed as a search model. Model-building and refinement were carried out using COOT[18] and REFMAC5,[19] respectively.

The second dataset was collected at SPring-8 with a 0.1-s exposure for 1.0° oscillation with a 0.3-mm aluminum attenuator using a wavelength of 1.000 Å X-ray for the low-resolution dataset, and with a 0.4-s exposure for 0.5° oscillation without the aluminum attenuator, using a wavelength of 0.85 Å X-ray for the high-resolution dataset. Integration was performed from 200 to 2.2 Å and from 2.5 to 0.96 Å for the low- and high-resolution datasets, respectively. The integrated intensities were scaled and merged into one dataset. Model building was carried out based on the partially refined structure using the initial dataset at Photon Factory. The structure was finally refined to crystallographic *R*- and R_{free} factors of 12.8% and 15.3% by employing anisotropic *B* factors, respectively. The coordinates and structural factors were deposited with the protein data bank under ID 2Z6W.

Table I
Crystallographic Statistics

Data statistics	
Space group	$P2_12_12_1$
Unit cell (Å)	
a	38.88
b	69.31
c	112.1
Resolution (Å)	200–0.96 (0.97–0.96)[a]
No. of observed reflections	501,337
No. of unique reflections	180,558
Completeness (%)	97.7 (96.6)[a]
R merge (%)	5.9 (41.4)[a]
$I/\sigma(I)$	18.6 (2.4)[a]
Refinement statistics	
Crystallographic *R* (%)	15.3
Free *R* (%)	12.9
No. of reflection	171,367
No. of test reflection	9131
No. of atoms[b]	3528
CypD	2812
CsA	179
Solvents (waters/citrates)	537
Average *B* value	8.23
RMSD from ideal values	
Bond lengths (Å)	0.017
Bond angles (°)	1.826
Ramachandran plot	
Favored (%)	84.7
Additional allowed (%)	14.6
Generously allowed (%)	0.7

[a]Values in parentheses are for the highest resolution shell.
[b]Atoms having alternate conformations are individually counted.

RESULTS AND DISCUSSION

Preparation of the crystallization sample

A K133I mutant of human CypD, instead of the wild-type enzyme, was employed to obtain the present crystal of the CypD-CsA complex, because it was reported that this mutant showed the reasonable solubility in water and the similar activity with the wild-type enzyme, and afforded crystals suitable for the X-ray work.[14]

CsA shows low solubility for water. CsA is usually soluble in organic solvents such as DMSO and ethanol, which are unsuitable for protein crystallization. We therefore prepared the CypD-CsA complex without the use of organic solvents, and instead utilized the high solubility of CypD in water and its strong affinity to CsA.

The addition of a small amount of CsA in ethanol to the aqueous CypD solution resulted in the immediate formation of white precipitants. This precipitation might have been CsA, the solubility of which is very low in water. However, the precipitation disappeared after 3 days of incubation. This result implied that CsA was

DOI 10.1002/prot

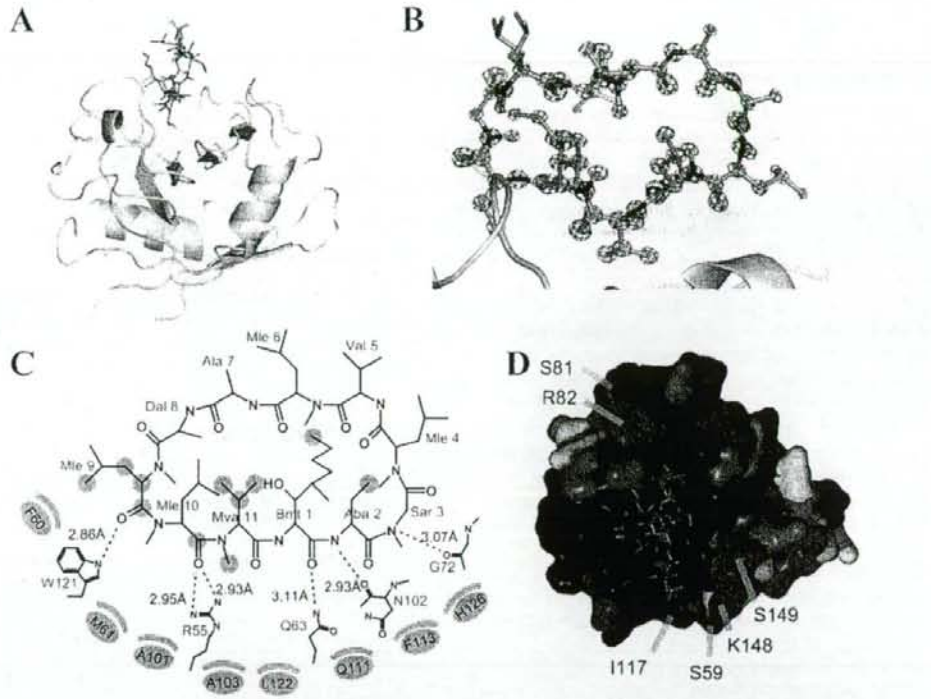

Figure 1

(A) Overall structure of CypD in complex with CsA. CypD and CsA are shown as ribbon- and stick-models, respectively. Panels A, B, and D were drawn with PyMOL (http://www.pymol.org). (B) Close-up view of CsA superimposed on its Fo-Fc omit electron density map (blue mesh) contoured at 6.0 σ. (C) Binding geometry of CsA on CypD. Green circles mark the CsA atoms involved in the hydrophobic contact with CypD. The CypD residues in green ellipsoids are involved in the hydrophobic interactions with CsA. The red dotted lines represent hydrogen bonding. This panel was prepared based on a scheme drawn with LIGPLOT.[21] Abbreviations of CsA residues: Bmt, (4R)-4[(E)-2-butenyl]-4,N-dimethyl-L-threonine; Abu: L-α-aminobutyric acid; Sar: sarcosine, Mle, N-methyl leucine; Dal, D-alanine; Mva, N-methyl valine. (D) Distribution of the conserved residues among human cyclophilins represented on the surface of the present CypD-CsA structure. Residues conserved in all five known human cyclophilins (CypA, CypB, CypC, CypD, and CypE) are shown in red. CypD residues conserved in 3 of 4, 2 of 4, and 1 of 4 other cyclophilins are shown in orange, yellow, and green, respectively, and the unconserved CypD residues in the other four cyclophilins are shown in blue. CsA is shown as a stick model.

soluble in the aqueous CypD solution, and that the CypD-CsA complex could be formed by the incubation of a CypD solution with CsA powders. In order to drive all CypD molecules in the solution to form a complex with CsA, excess CsA was added to the aqueous CypD solution and the mixture was incubated for 5 days. As described in the following paragraph, the crystal structure indicated that the CypD-CsA complex was successfully formed according to this protocol, which can be applied for the crystallization of protein–ligand complexes with various water-insoluble ligands.

Structure determination

The structure of the CypD-CsA complex was refined at 0.96-Å resolution; the present resolution is the highest among those of known Cyp crystal structures. As the highest resolution of previously known Cyp-complex structures was 1.5 Å,[20] the present structure provides additional details regarding the mode of binding between Cyp and CsA. The present crystals belong to the orthorhombic space group $P2_12_12_1$ with the unit cell dimensions of a = 40.71 Å, b = 72.97 Å, and c = 112.0 Å. The present crystal form differs from that of the apo-CypD crystals ($P4_12_12$).[14] Two CypD-CsA complexes are found in an asymmetric unit of the present crystal; the Matthews coefficient, V_m, and the solvent content are calculated to be 2.0 Å^3/Da and 38.2%, respectively. Multi-conformations are assigned for 42 amino acid residues in the structural model, among a total of 328 amino acid residues of the two CypD molecules in an asymmetric

unit. The data collection and refinement statistics are summarized in Table I.

Overall structure

The structure of human CypD is composed of eight β-strands, two α-helices, and one 3_{10} helix [Fig. 1(A)], and this structure is similar to that of the other known cyclophilin structures. The RMSDs between the Cα atoms of the present structure and those of CypA-CsA, CypB-CsA, CypC-CsA, and CypE(apo) are 0.50 Å (for 164 atoms), 0.67 Å (159 atoms), 0.68 Å (158 atoms), and 0.68 Å (161 atoms), respectively.

The F_o-F_c map phased only with the CypD structure showed additional clear electron densities corresponding to the CsA molecule, confirming that the crystal was composed of the CypD-CsA complex [Fig. 1(B)]. The averaged *B*-factors of CypD and CsA are 6.7 $Å^2$ (2812 nonhydrogen atoms) and 6.5 $Å^2$ (179 nonhydrogen atoms), respectively. This suggests that the CsA molecule is rigidly bound to the CypD molecule to form the stable CypD-CsA complex. This finding is consistent with the very strong affinity of CsA to CypD (K_D= 13.4 n*M*).[14] The CypD structure in the present complex is very similar to that of apo-CypD (RMSD of Cα = 0.48 Å for 164 atoms), suggesting that CypD does not need to undergo a conformational change in order to bind with CsA, in spite of the fact that CsA (1.2 kDa) has one-fifteenth of the molecular weight of CypD (17.8 kDa).

The mutated Ile133 was involved in the important intermolecular contacts in the apocrystal.[14] In the present crystal composed of two CypD-CsA complexes in an asymmetric unit, one of the two CypD complexes makes no contact with the other complex via Ile133, but Ile133 on the other CypD molecule is directly involved in the intercomplex interaction. Therefore, wild-type CypD is not considered to form the present crystal packing arrangement found in the case of apo-CypD.

Binding with CsA

The binding mode of CsA with CypD is shown on Figure 1(C). One-half of CsA residues (Sar3-Dal8) is exposed to the solvent region and the other half (Bmt1, Aba2, and Mle9-Mva11) is buried in the CypD molecule. Since CsA is a cyclic peptide composed of hydrophobic residues, the molecule interacts with CypD primarily via hydrophobic contacts. Hydrogen bonds are formed only using main-chain N and O atoms of CsA [Fig. 1(C)].

The amino-acid sequence identities of CypD with CypA, CypB, CypC, and CypE are 75%, 61%, 58%, and 67%, respectively. These highly conserved residues are distributed across the molecular surface, as shown in Figure 1(D). All residues in contact with CsA are completely conserved in all human cyclophilins. The PPIase active site is known to be located at the bottom of the CsA binding site. Residues Ser59, Ser81, Arg82, Ile117, Lys148, and Ser149 of CypD are located around the CsA binding site, and they are not well conserved in the other cyclophilins (CypA, CypB, CypC, and CypE). These residues are thought to specifically recognize the ligand proteins. Molecules that bind to these residues could be a leading compound as CypD-specific inhibitors, and they may therefore serve as potential targets for the development of anti-infarction drugs.

ACKNOWLEDGMENTS

We appreciate the help of Drs. M. Kawamoto and N. Shimizu of SPring-8 and Drs. N. Igarashi, N. Matsugaki, and Y. Yamada of Photon Factory with the X-ray diffraction experiments.

REFERENCES

1. Fischer G, Wittmann-Liebold B, Lang K, Kiefhaber T, Schmid FX. Cyclophilin and peptidyl-prolyl *cis-trans* isomerase are probably identical proteins. Nature 1989;337:476–478.
2. Galat A, Metcalfe SM. Peptidylproline *cis/trans* isomerases. Prog Biophys Mol Biol 1995;63:67–118.
3. Takahashi N, Hayano T, Suzuki M. Peptidyl-prolyl *cis-trans* isomerase is the cyclosporin A-binding protein cyclophilin. Nature 1989;337: 473–475.
4. Trandinh CC, Pao GM, Saier MH, Jr. Structural and evolutionary relationships among the immunophilins: two ubiquitous families of peptidyl-prolyl *cis-trans* isomerases. Faseb J 1992;6:3410–3420.
5. Price ER, Zydowsky LD, Jin MJ, Baker CH, McKeon FD, Walsh CT. Human cyclophilin B: a second cyclophilin gene encodes a peptidyl-prolyl isomerase with a signal sequence. Proc Natl Acad Sci USA 1991;88:1903–1907.
6. Spik G, Haendler B, Delmas O, Mariller C, Chamoux M, Maes P, Tartar A, Montreuil J, Stedman K, Kocher HP, Kellers R, Hiestand PC, Movva NR. A novel secreted cyclophilin-like protein (SCYLP). J Biol Chem 1991;266: 10735–10738.
7. Halestrap AP, McStay GP, Clarke SJ. The permeability transition pore complex: another view. Biochimie 2002;84:153–166.
8. Nakagawa T, Shimizu S, Watanabe T, Yamaguchi O, Otsu K, Yamagata H, Inohara H, Kubo T, Tsujimoto Y. Cyclophilin D-dependent mitochondrial permeability transition regulates some necrotic but not apoptotic cell death. Nature 2005;434:652–658.
9. Baines CP, Kaiser RA, Purcell NH, Blair NS, Osinska H, Hambleton MA, Brunskill EW, Sayen MR, Gottlieb RA, Dorn GW, Robbins J, Molkentin JD. Loss of cyclophilin D reveals a critical role for mitochondrial permeability transition in cell death. Nature 2005;434: 658–662.
10. Schinzel AC, Takeuchi O, Huang Z, Fisher JK, Zhou Z, Rubens J, Hetz C, Danial NN, Moskowitz MA, Korsmeyer SJ. Cyclophilin D is a component of mitochondrial permeability transition and mediates neuronal cell death after focal cerebral ischemia. Proc Natl Acad Sci USA 2005;102:12005–12010.
11. Broekemeier KM, Dempsey ME, Pfeiffer DR. Cyclosporin A is a potent inhibitor of the inner membrane permeability transition in liver mitochondria. J Biol Chem 1989;264:7826–7830.
12. Mikol V, Kallen J, Pflugl G, Walkinshaw MD. X-ray structure of a monomeric cyclophilin A-cyclosporin A crystal complex at 2.1 Å resolution. J Mol Biol 1993;234:1119–1130.
13. Mikol V, Kallen J, Walkinshaw MD. X-ray structure of a cyclophilin B/cyclosporin complex: comparison with cyclophilin A and delinea-

DOI 10.1002/prot

tion of its calcineurin-binding domain. Proc Natl Acad Sci USA 1994;91:5183–5186.
14. Schlatter D, Thoma R, Kung E, Stihle M, Muller F, Borroni E, Cesura A, Hennig M. Crystal engineering yields crystals of cyclophilin D diffracting to 1.7 Å resolution. Acta Crystallogr Sect D 2005; 61 (Part 5):513–519.
15. Otwinowski Z, Minor W. Processing of X-ray diffraction data collected in oscillation mode. In: Carter CW, Jr, Sweet RM, editors. Macromolecular crystallography, Part A: Methods in enzymology, Vol. 276. New York: Academic Press; 1997. pp 307–326.
16. Collaborative Computional Project N. The CCP4 suite: programs for protein crystallography. Acta Crystallogr Sect D 1994;50:760–763.
17. Vagin A, Teplyakov A. MOLREP: an automated program for molecular replacement. J Appl Crystallogr 1997;30:1022–1025.
18. Emsley P, Cowtan K. Coot: model-building tools for molecular graphics. Acta Crystallogr Sect D 2004;60 (Part 12, Part 1):2126–2132.
19. Murshudov GN, Vagin AA, Lebedev A, Wilson KS, Dodson EJ. Efficient anisotropic refinement of macromolecular structures using FFT. Acta Crystallogr Sect D 1999;55 (Part 1):247–255.
20. Glaser AG, Limacher A, Fluckiger S, Scheynius A, Scapozza L, Crameri R. Analysis of the cross-reactivity and of the 1.5 Å crystal structure of the *Malassezia sympodialis* Mala s 6 allergen, a member of the cyclophilin pan-allergen family. Biochem J 2006;396: 41–49.
21. Wallace AC, Laskowski RA, Thornton JM. LIGPLOT: a program to generate schematic diagrams of protein–ligand interactions. Protein Eng 1995;8:127–134.

balt6/zns-neusci/zns-neusci/zns00908/zns4528-08a | slaterl | S=7 | 2/18/08 | 15:16 | Art: 3323393 | Input-YY(v)

The Journal of Neuroscience, February 27, 2008 · 28(9):●–● · 1

Neurobiology of Disease

Neuroaxonal Dystrophy Caused by Group VIA Phospholipase A_2 Deficiency in Mice: A Model of Human Neurodegenerative Disease

AQ: A

Koei Shinzawa,[1] Hisae Sumi,[2] Masahito Ikawa,[3] Yosuke Matsuoka,[1] Masaru Okabe,[3] Saburo Sakoda,[2] and Yoshihide Tsujimoto[1]

[1]Department of Medical Genetics, Laboratory of Molecular Genetics and Solution-Oriented Research for Science and Technology, Japan Science and Technology Agency, and [2]Department of Neurology, Osaka University Medical School, Osaka 565-0871, Japan, and [3]Research Institute for Microbial Diseases, Osaka University, Osaka 565-0871, Japan

Calcium-independent group VIA phospholipase A_2 (iPLA$_2\beta$) is considered to play a role in signal transduction and maintenance of homeostasis or remodeling of membrane phospholipids. A role of iPLA$_2\beta$ has been suggested in various physiological and pathological processes, including immunity, chemotaxis, and cell death, but the details remain unclear. Accordingly, we investigated mice with targeted disruption of the *iPLA$_2\beta$* gene. *iPLA$_2\beta^{-/-}$* mice developed normally and grew to maturity, but all showed evidence of severe AQ: B motor dysfunction, including a hindlimb clasping reflex during tail suspension, abnormal gait, and poor performance in the hanging wire grip test. Neuropathological examination of the nervous system revealed widespread degeneration of axons and/or synapses, accompanied by the presence of numerous spheroids (swollen axons) and vacuoles. These findings provide evidence that impairment of *iPLA$_2\beta$* causes neuroaxonal degeneration, and indicate that the *iPLA$_2\beta^{-/-}$* mouse is an appropriate animal model of human neurodegenerative AQ: C diseases associated with mutations of the *iPLA$_2\beta$* gene, such as infantile neuroaxonal dystrophy and neurodegeneration with brain iron accumulation.

Key words: phospholipase; neurodegeneration; neuroaxonal dystrophy; knock-out mouse; iPLA$_2$; spheroid

Introduction

AQ: D The phospholipases A_2 (PLA$_2$) comprise a family of esterases that hydrolyze the *sn-2* ester bond in phospholipids to yield free fatty acids and lysophospholipids. A number of PLA$_2$ isotypes have been identified in mammals, and depending on their subcellular localization and enzymatic properties, these are divided into three major subfamilies, which are secretory PLA$_2$ (sPLA$_2$), cytosolic Ca^{2+}-dependent PLA$_2$ (cPLA$_2$), and Ca^{2+}-independent PLA$_2$ (iPLA$_2$) (Six and Dennis, 2000; Ma and Turk, 2001). The sPLA$_2$s are extracellular enzymes with a low molecular mass (~14 kDa) that require millimolar concentrations of Ca^{2+} for activation. sPLA$_2$s are thought to be potent mediators of inflammation and also show antibacterial activity. In contrast, the cPLA$_2$s are intracellular enzymes that specifically target arachidonic acid at the *sn-2* position of phospholipids. Their activity is regulated by submicromolar levels of Ca^{2+}, and these enzymes are believed to play a pivotal role in the production of arachidonic acid metabolites, such as eicosanoids. The iPLA$_2$s do not require Ca^{2+} for their catalytic activity and are suggested to be involved in remodeling of membrane phospholipids as well as in various cellular signaling processes. In mammals, two iPLA$_2$ genes (iPLA$_2\beta$ and iPLA$_2\gamma$) have been cloned (Tang et al., 1997; Mancuso et al., 2000).

The physiological role of the PLA$_2$s in the nervous system remains largely unknown in mammals. To our knowledge, there have been no previous reports about neurological dysfunction in PLA$_2$ knock-out mice. The *iPLA$_2\beta$* gene is expressed in all regions of the mammalian brain and iPLA$_2$ is the dominant PLA$_2$ activity in rat brain cytosol (Yang et al., 1999; Balboa et al., 2002). Accumulated evidence suggests that changes of phospholipids may be to associated with cell death, including apoptosis and necrosis (caspase-independent cell death) (Shinzawa and Tsujimoto, 2003), and may cause many neurodegenerative diseases, including cerebral infarction and Alzheimer disease (Farooqui et al., 2004). Moreover, it was very recently reported that *iPLA$_2\beta$* gene mutations occur in several human neurodegenerative disorders, such as infantile neuraxonal dystrophy (INAD) and neurodegeneration with brain iron accumulation (NBIA) (Khateeb et al., 2006; Morgan et al., 2006), which are all pathologically characterized by widespread development of axonal swellings (spheroids) in the central and peripheral nervous systems, suggesting that

Received Nov. 22, 2006; revised Jan. 15, 2008; accepted Jan. 17, 2008.

This work was supported in part by a grant from the 21st Century Center of Excellence Program, a Scientific Research grant from the Japanese Ministry of Education, Science, Sports, and Culture, and a Comprehensive Research on Aging and Health grant from the Ministry of Health, Labor and Welfare, Japan. We are grateful to Y. Maruyama, A. Kawai, T. Aikawa, K. Ideguchi, and Y. Haseda for technical assistance and Drs. S. Kato and M. Etoh for AQ: L their helpful advice.

Correspondence should be addressed to Yoshihide Tsujimoto, Laboratory of Molecular Genetics, Osaka University Medical School, Room 88, 2-2 Yamadaoka, Suita, Osaka 565-0871, Japan. E-mail: tsujimot@gene.med.osaka-u.ac.jp.

DOI:10.1523/JNEUROSCI.4354-07.2008

 0270-6474/08/280001-♦$15.00/0

balt6/zns-neusci/zns-neusci/zns00908/zns4528-08a | slaterl | S=7 | 2/18/08 | 15:16 | Art: 3323393 | Input-YY(v)

impairment of *iPLA$_2\beta$* is involved in the pathogenesis of neuroaxonal dystrophy.

To explore the physiological and pathological role of *iPLA$_2\beta$*, we generated *iPLA$_2\beta^{-/-}$* mice. Here, we report that *iPLA$_2\beta^{-/-}$* mice developed motor dysfunction associated with prominent formation of spheroids and vacuoles in axons and synapses throughout the nervous system. These findings provide evidence that impairment of *iPLA$_2\beta$* causes neuroaxonal dystrophy.

Materials and Methods

Animal. The C57BL/6 mice used in this study were obtained from Japan SLC (Shizuoka, Japan). The experimental protocol was approved by the Ethical Review Committee for Animal Experimentation of Osaka University Medical School.

In situ *hybridization.* An RNA probe was prepared by *in vitro* transcription, as described previously (Matsuoka et al., 2002), using digoxigenin (DIG)-UTP and the pGEM-T easy plasmid vector (Promega, Madison, WI) carrying 720 bases (1732–2452) of mouse iPLA$_2\beta$ cDNA.

Brains, spinal cords, and dorsal root ganglia of the mice were dissected, submerged in OCT Tissue-Tek mounting medium (Miles, Elkhart, IN), and rapidly frozen at −40°C in 2-methyl-butane. Sections 7 μm thick were cut on a cryostat and mounted on Matsunami adhesive silane-coated slides (Matsunami, Osaka, Japan). Refixation, acetylation, and hybridization of the sections were performed as described previously (Zhong et al., 2004). After washing three times with 50% formamide and 2× SSC at 60°C, the sections were treated with blocking reagent for 30 min at room temperature, and then incubated with alkaline phosphatase-conjugated anti-DIG antibody for 30 min. After washing three times, the sections were incubated in 100 mM Tris-HCl, pH 9.5, 100 mM NaCl, 0.03% nitro blue tetrazolium, and 0.015% bromochloroindoyl phosphate. Then, color development was stopped by incubation in PBS containing 10 mM EDTA, after which the sections were treated in 100% ethanol and xylene, and then embedded for microscopic observation.

Targeted disruption of the iPLA$_2\beta$ *gene.* A vector for disruption of the *iPLA$_2\beta$* gene was constructed using genomic DNA derived from 129/Sv embryonic stem (ES) cells and the pMulti-ND-1.0 vector (Inoue et al., 2005). Briefly, a 2.3 kb genomic fragment containing exon 10 and a 7.7 kb genomic fragment containing exons 5–8 were inserted into the *Pac*I site and the *Cla*I site of the vector, respectively.

ES cells [clone D3 (p13GIRC)] were transfected with the vector, and neomycin-resistant clones were isolated. After screening 288 resistant clones by PCR and subsequently by Southern blot analysis of *Bgl*II-digested genomic DNA using a probe A or a probe B, two ES cells lines with disruption of the *iPLA$_2\beta$* gene were obtained. These ES cells were injected into C57BL/6 blastocysts to produce chimeric mice, which were crossed with C57BL/6 mice to obtain *iPLA$_2\beta^{+/-}$* F1 progeny. The littermates obtained from pairing of *iPLA$_2\beta^{+/-}$* F2 mice were pooled and used for this study.

Genotyping of mice by PCR and Southern blot analysis. Genomic DNA was prepared from mouse tails. To amplify the wild-type and disrupted *iPLA$_2\beta$* loci, the following primers were used: wild-type (349 bp), ATGGATCCGTGGTCTTCATCTACCTCCTCG and TGAGCCCAATGCTAGGAATGTCCAATCAGC; disrupted *iPLA$_2\beta$* locus (480 bp), TGGCGGACCGCTATCAGGACATAGCGTTGG and AGGTGGAGTGCAGGAACAAGGCCTATCAGG.

The PCR was performed using a Gene *Taq* (Nippon Gene, Tokyo, Japan), with 32 cycles of 95°C for 30 s, 63°C for 30 s, and 72°C for 1 min. Southern blot analysis was performed using a Gene Images kit (GE Healthcare Bio-Science, Piscataway, NJ). The probes were prepared by PCR using a dNTP mixture containing fluorescein-11-dUTP and the following primes: probe A (423 bp), GCCGGCCTGAACCAGGTAAACAACCAAGGG and TGACCTGCCAAGCAGCAGACTCAAGAGCAG; probe B (777 bp), TCAAGAAGGCGATAGAAGGCGATGCGCTGC and TGAACAAGATGGATTGCACGCAGGTTCTCC. Hybridization, washing, and detection were performed according to the supplier's protocol.

Western blot analysis. Testes obtained from male mice were homogenized with radioimmunoprecipitation assay buffer (50 mM Tris-HCl, pH 7.4, 150 mM NaCl, 1% Nonidet P-40, 0.5% sodium deoxycholate, 0.1% SDS, and protease inhibitor mixture). As described previously (Shinzawa and Tsujimoto, 2003), immunoblot analysis was performed with a polyclonal anti-iPLA$_2\beta$ antibody (Cayman Chemical, Ann Arbor, MI) or a monoclonal anti-α-tubulin antibody (clone B-5-1-2) (Sigma, St. Louis, MO) and an HRP-conjugated secondary antibody using ECL Western blotting detection reagents (GE Healthcare Bio-Science).

Behavioral analysis. The hanging wire grip test was performed by placing a mouse on a wire net and then turning the net upside down at a height of ~20 cm above the cage floor to prevent the animal from easily climbing down. The time that elapsed until the animal fell was recorded three times and the cutoff time was set at 60 s. Footprint patterns were obtained by painting the forepaws and the hindpaws with blue and red ink, respectively.

Histochemical and immunohistochemical analysis. Mice aged 95–103 weeks (*iPLA$_2\beta^{+/+}$*, one male and three females; and *iPLA$_2\beta^{-/-}$*, three males and four females), mice aged 56 weeks (*iPLA$_2\beta^{+/+}$*, one female;

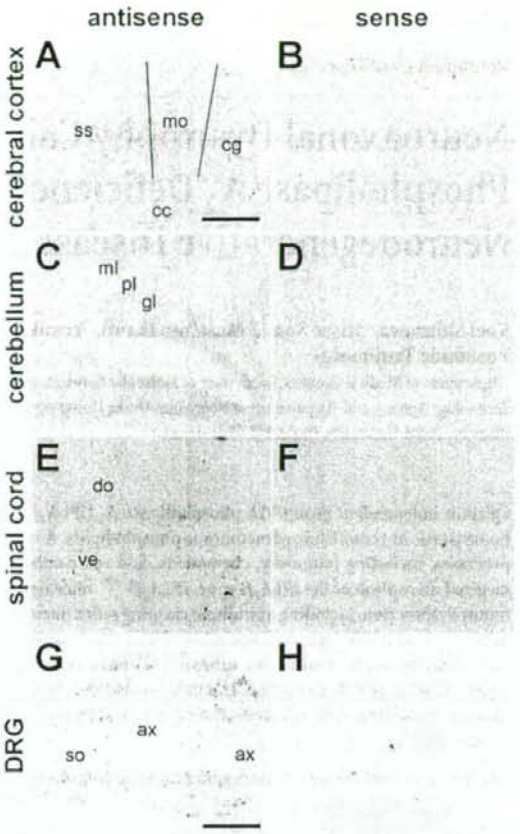

Figure 1. *In situ* hybridization of iPLA$_2\beta$ mRNA in the nervous system. ***A–H***, The pattern of iPLA$_2\beta$ mRNA expression in the cerebral cortex (***A***, ***B***), the cerebellum (***C***, ***D***), the spinal cord (***E***, ***F***), and the dorsal root ganglion (DRG) (***G***, ***H***) of 7-week-old female mice. The antisense probe detected signals in all cortical layers, except for layer I, of the cingulate (cg), the motor (mo) cortex, and the somatosensory (ss) cortex, in the Purkinje cell layer (pl) and the granular layer (gl), but not the molecular layer (ml) of the cerebellum, in the dorsal (do) and ventral (ve) horns of the spinal cord, and the soma-rich region of the DRG (so). No signals were detected in the corpus callosum (cc) or in the axon-rich region (ax) that contains mainly axons and oligodendrocytes (cc) or Schwann cells (ax). The sense probe was used as a negative control (***B***, ***D***, ***F***, ***H***). Scale bars: ***A–F***, 500 μm; ***G***, ***H***, 180 μm.

balt6/zns-neusci/zns-neusci/zns00908/zns4528-08a | slaterl | S=7 | 2/18/08 | 15:16 | Art: 3323393 | Input-YY(v)

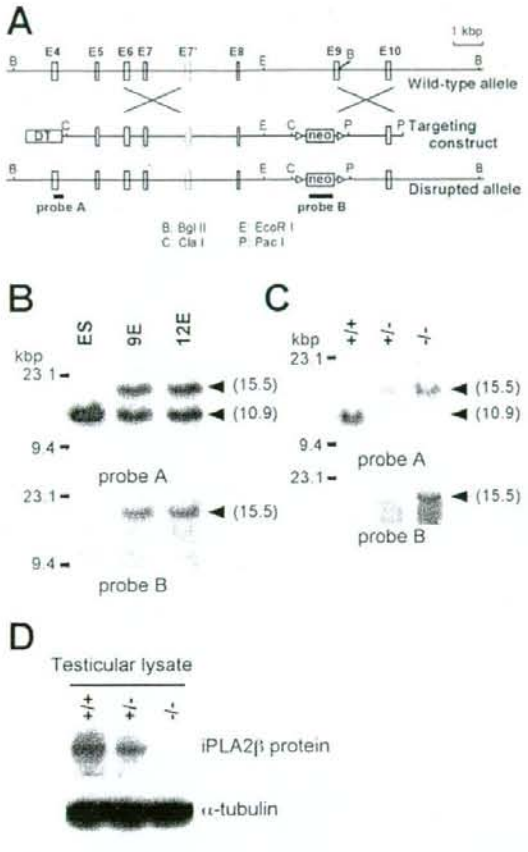

Figure 2. Targeting the *iPLA$_2\beta$* gene. ***A***, Diagram of the wild-type *iPLA$_2\beta$* gene, the targeting construct, and the disrupted *iPLA$_2\beta$* allele. ***B***, ***C***, Southern blot analysis of *Bgl*II-digested genomic DNA from ES cell clones (***B***) and from the tails of *iPLA$_2\beta^{+/+}$*, *iPLA$_2\beta^{+/-}$*, and *iPLA$_2\beta^{-/-}$* mice (***C***). The DNA probes used for Southern blot analysis were a probe A and B containing exon 4 and neomycin resistance gene (neo), respectively. The *iPLA$_2\beta^{+/+}$* wild-type allele generated a band of 10.9 kbp, whereas the disrupted allele yielded a 15.5 kbp fragment. ***D***, Western blotting of testicular lysates with an anti-iPLA$_2\beta$ antibody (α-tubulin was used as the loading control).

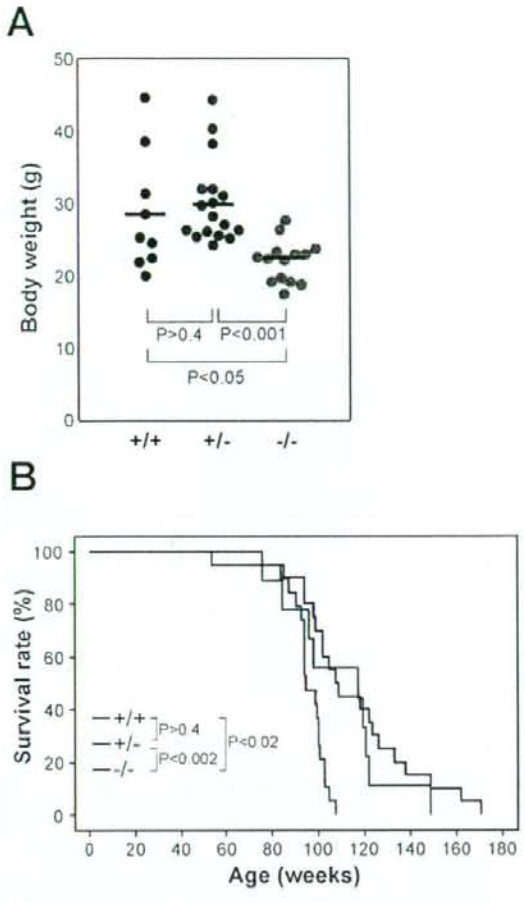

Figure 3. Lower body weight and shorter lifespan of *iPLA$_2\beta^{-/-}$* mice. ***A***, Body weight of female *iPLA$_2\beta^{+/+}$* mice ($n = 9$), *iPLA$_2\beta^{+/-}$* mice ($n = 17$), and *iPLA$_2\beta^{-/-}$* mice ($n = 14$) at 91–100 weeks of age. Bars indicate the mean values. p values were calculated using the Student's t test. ***B***, Survival of female *iPLA$_2\beta^{+/+}$* mice ($n = 9$), *iPLA$_2\beta^{+/-}$* mice ($n = 20$), and *iPLA$_2\beta^{-/-}$* mice ($n = 19$). p values were calculated using the log-rank test. Results obtained with male mice were virtually identical.

and *iPLA$_2\beta^{-/-}$*, four females), mouse aged 32 weeks (*iPLA$_2\beta^{-/-}$*, one female), and mice aged 15 weeks (*iPLA$_2\beta^{-/-}$*, one male and one female) were used for histological examination. After being treated with an overdose of sodium pentobarbital, each animal was perfused with PBS and then 4% paraformaldehyde. The brain, spinal cord, and sciatic nerve were removed from each mouse, immersed in the same fixative overnight at 4°C, and then dehydrated and embedded in paraffin blocks. Then 4-μm-thick paraffin sections were prepared and stained with hematoxylin and eosin (H&E), Nissl, Luxol fast blue, periodic acid-Shiff (PAS), Bielschowsky, or Berlin blue stain. Small pieces of sciatic nerves from mice aged 95–103 weeks and the cerebral cortex and the dorsal part of the cervical spinal cord from mice aged 56 weeks were fixed with 2.5% glutaraldehyde and processed to Epon blocks as described previously (Sumi et al., 2006). Transverse Epon sections, 1 μm thick, of sciatic nerves were stained with toluidine blue.

To perform immunohistochemistry, deparaffinized sections were processed as described previously (Sumi et al., 2006). The antibodies used were a mouse monoclonal antibody for phosphorylated neurofilament (Covance, Berkeley, CA) and rabbit polyclonal antibody for ubiquitin (Dako, Glostrup, Denmark). Hematoxylin was used to counterstain the cell nuclei.

To estimate the total density of myelinated nerve fibers in the sciatic nerve per unit area, three images of the large nerve fascicles (100× objective, 62,080 μm^2) were obtained with a digital camera (VB-7010; Keyence, Osaka, Japan) attached to a light microscope (Eclipse E800; Nikon, Tokyo, Japan), and the number of myelinated fibers in the four images was counted in each mouse. To estimate the area of the sciatic nerves, images of the whole nerve (10× objective) were obtained with a digital camera attached to the light microscope, and the areas of all nerve fascicles were measured using image analysis software (VH-H1A5; Keyence). The total number of myelinated fibers in the sciatic nerve was calculated from the density and the area.

Ultrathin sections of the cerebral cortex and the dorsal horn were cut and stained with uranyl acetate and lead citrate, and were examined by transmission electron microscopy (H-7650; Hitachi, Tokyo, Japan).

balt6/zns-neusci/zns-neusci/zns00908/zns4528-08a | slaterl | S=7 | 2/18/08 | 15:16 | Art: 3323393 | Input-YY(v)

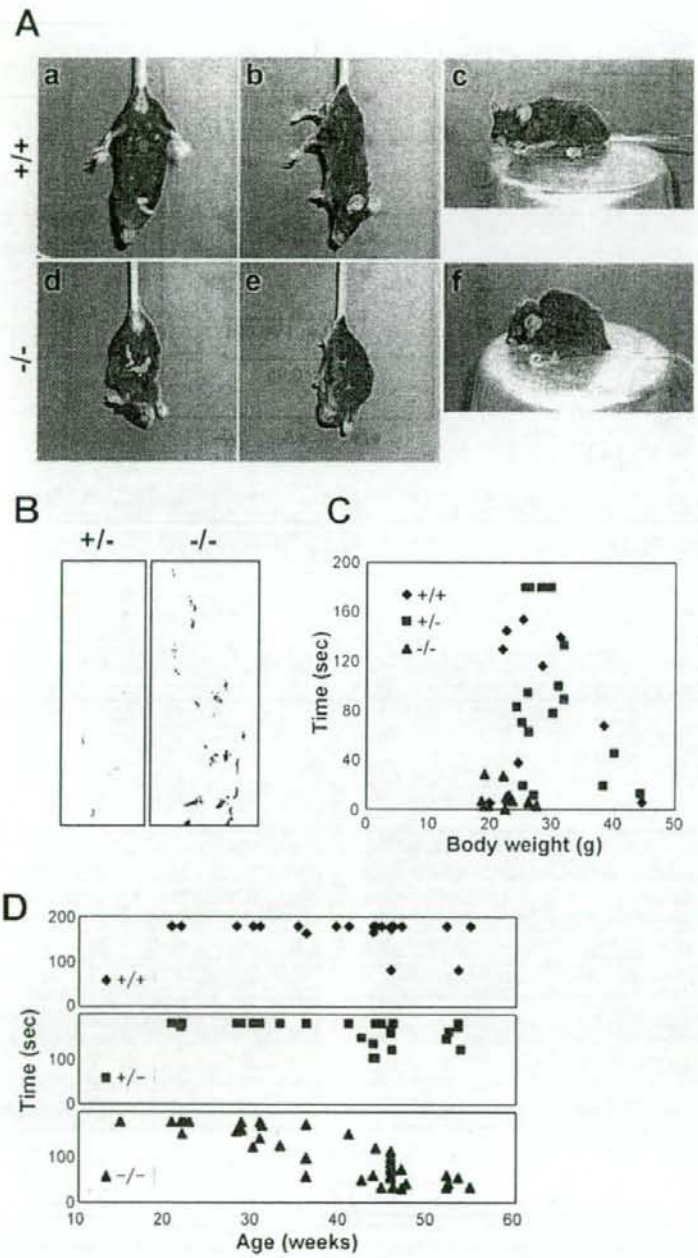

Figure 4. Motor dysfunction in *iPLA$_2\beta^{-/-}$* mice. ***A***, Representative photographs of an *iPLA$_2\beta^{+/+}$* mouse (***a–c***) and an *iPLA$_2\beta^{-/-}$* mouse (***d–f***) at 95 weeks of age. The *iPLA$_2\beta^{-/-}$* mouse adopts a feet-clasping posture when suspended by the tail (***d***, ***e***), whereas the *iPLA$_2\beta^{+/+}$* mouse holds its hindlimbs outward to steady itself (***a***, ***b***). The *iPLA$_2\beta^{-/-}$* mouse has a hunched posture (***f***). ***B***, Representative footprint patterns of *iPLA$_2\beta^{+/-}$* and *iPLA$_2\beta^{-/-}$* mice at 90 and 87 weeks of age, respectively. Forepaws and hindpaws were painted with blue and red ink, respectively. The *iPLA$_2\beta^{-/-}$* mouse displays an irregular stride and dragging of the hindlimbs. ***C***, ***D***, Hanging wire grip test. ***C***, Female *iPLA$_2\beta^{+/+}$* mice ($n = 9$), *iPLA$_2\beta^{+/-}$* mice ($n = 17$), and *iPLA$_2\beta^{-/-}$* mice ($n = 13$) (91–100 weeks old) were tested as described in Materials and Methods, and the total time for three trials was plotted against body weight. ***D***, Female *iPLA$_2\beta^{+/+}$* mice ($n = 23$), *iPLA$_2\beta^{+/-}$* mice ($n = 25$), and *iPLA$_2\beta^{-/-}$* mice ($n = 42$) (15–55 weeks old) were tested. The total time for three trials was plotted against age.

Results

Expression of *iPLA$_2\beta$* mRNA in the nervous system

As described below, *iPLA$_2\beta^{-/-}$* mice suffered from neurodegeneration. Accordingly, we performed detailed examination of the pattern of *iPLA$_2\beta$* gene expression in the nervous system by *in situ* hybridization. Because of unavailability of suitable anti-iPLA$_2\beta$ antibody, we were unable to perform immunohistochemical analysis. As shown in Figure 1*A*, every layer of the cerebral cortex, except for layer I, was stained by the antisense probe for the *iPLA$_2\beta$* gene, but not by the sense probe (Fig. 1*B*). No signals were detected in the corpus callosum where axons and oligodendrocytes are prominent. In the cerebellum, weak *iPLA$_2\beta$* gene expression was seen in the granular layer, whereas there was stronger expression in the Purkinje cells (Fig. 1*C*). In the spinal cord, both dorsal and ventral horn neurons showed strong expression of the *iPLA$_2\beta$* gene (Fig. 1*E*). Moreover, dorsal root ganglion cells showed somatic expression of *iPLA$_2\beta$*, although there was no expression in their axons or in the Schwann cells (Fig. 1*G*). Together, these results indicated that the *iPLA$_2\beta$* gene was widely expressed by neurons.

Generation of *iPLA$_2\beta^{-/-}$* mice

To evaluate the physiological role of *iPLA$_2\beta$*, we generated mice with targeted disruption of the *iPLA$_2\beta$* gene. As described in Figure 2*A*, a targeting vector was designed, so that exon 9 (which encodes the catalytic domain including the active center amino acid residue, Ser 465) was replaced by a neomycin resistance gene (neo) cassette. Following the standard procedure described in Materials and Methods, two ES cell lines (9E and 12E) with the disrupted allele were obtained (Fig. 2*B*) and then injected into blastocysts to produce chimeric mice. One of the two cell lines (9E) transmitted the disrupted allele to the germline. *iPLA$_2\beta^{+/-}$* mice were interbred to generate *iPLA$_2\beta^{-/-}$* mice and their offspring were genotyped by PCR and Southern blot analysis (Fig. 2*C*). The absence of iPLA$_2\beta$ protein in *iPLA$_2\beta^{-/-}$* mice was confirmed by Western blot analysis using testicular lysates (Fig. 2*D*), indicating that the disrupted allele was a null mutation. The ratio of offspring with each genotype was in accordance with the Mendelian rule (*iPLA$_2\beta^{+/+}$*:*iPLA$_2\beta^{+/-}$*:*iPLA$_2\beta^{-/-}$* = 81:141:67). *iPLA$_2\beta^{-/-}$* mice developed normally and grew to maturity. Male mice exhibited reduced fertility (data

balt6/zns-neusci/zns-neusci/zns00908/zns4528-08a | slaterl | S=7 | 2/18/08 | 15:16 | Art: 3323393 | Input-YY(v)

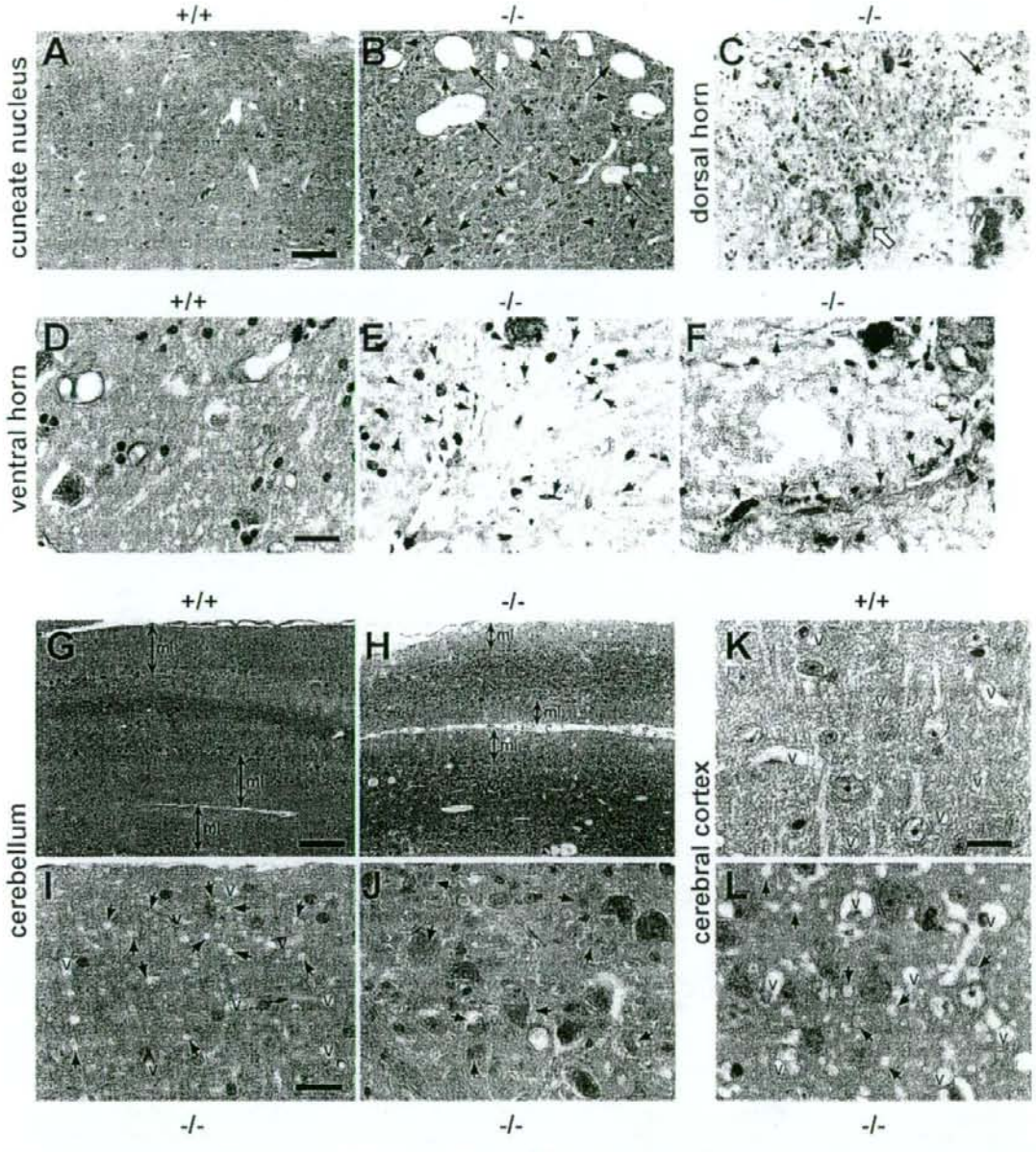

Figure 5. Neuropathological changes in $iPLA_2\beta^{-/-}$ mice. ***A***, ***B***, Cuneate nucleus of an $iPLA_2\beta^{+/+}$ mouse (***A***) and an $iPLA_2\beta^{-/-}$ mouse (***B***) at 2 years (95–103 weeks old). ***C***, Dorsal horn of $iPLA_2\beta^{-/-}$ mouse at 2 years. ***D–F***, Ventral horn of an $iPLA_2\beta^{+/+}$ mouse at 56 weeks (***D***) and an $iPLA_2\beta^{-/-}$ mouse at 15 weeks (***E***) and 2 years (***F***). ***G***, ***H***, Cerebellum of an $iPLA_2\beta^{+/+}$ mouse (***G***) and an $iPLA_2\beta^{-/-}$ mouse (***H***) at 2 years. ***I***, ***J***, Molecular layer (***I***) and dentate nucleus (***J***) of the cerebellum of an $iPLA_2\beta^{-/-}$ mouse at 15 weeks. ***K***, ***L***, Cerebral cortex of an $iPLA_2\beta^{+/+}$ mouse (***K***) and an $iPLA_2\beta^{-/-}$ mouse (***L***) at 2 years. ***A***, ***B***, ***G–L***, H&E stain. ***C–F***, PAS stain. ***A***, No spheroids and vacuoles are detected in the $iPLA_2\beta^{+/+}$ mouse. ***B***, Many spheroids (arrows) and large vacuoles (large arrows) can be observed. ***C***, Irregular PAS-positive spheroids (small arrows) contain fissures, vacuoles, and PAS-positive granules. The extent of PAS staining is variable. The core of the huge vacuole contains PAS-positive granules (large arrow and open arrow; also shown at a higher magnification). ***D***, No PAS-positive granules are observed in the $iPLA_2\beta^{+/+}$ mouse. ***E***, Strongly PAS-positive granules can be seen in normal-looking axons or the neuropil. ***F***, PAS-positive granules (arrows) in swollen axons. ***G***, ***H***, The molecular layer (ml) of the cerebellum from the $iPLA_2\beta^{-/-}$ mouse (***H***) is thinner than that from the $iPLA_2\beta^{+/+}$ mouse (***G***). ***I***, Numerous tiny vacuoles (arrows) can be seen in the molecular layer. ***J***, There are only a few spheroids (arrows). ***K***, There are no detectable vacuoles in the $iPLA_2\beta^{+/+}$ mouse. ***L***, Numerous small vacuoles (arrows) can be observed, but there are no spheroids. Scale bars: ***A–C***, 50 μm; ***D–F***, ***I–L***, 16 μm; ***G***, ***H***, 100 μm. v, Vessels.

balt6/zns-neusci/zns-neusci/zns00908/zns4528-08a | slaterl | S=7 | 2/18/08 | 15:16 | Art: 3323393 | Input-YY(v)

Table 1. Distribution of spheroids and vacuoles in the CNS

Region	Spheroids	Vacuoles
Cuneate nucleus	+++	++
Gracile nucleus	+++	++
Trigeminal nucleus	+++	++
Facial nucleus	++	+
Cochlear nucleus	+++	++
Vestibular nucleus	+++	++
Hypoglossal nucleus	+	+
Spinal cord		
dorsal horn	+++	++
ventral horn	++	++
dorsal funiculus	++	++
ventral funiculus	++	++
Striatum	+	++
Thalamus	+	++
Hypothalamus	+	++
Hippocampus	+	++ (small)[a]
Amygdala	+	++
Cerebellum		
molecular layer	+	++ (small)[a]
granular layer	+	++
dentate nucleus	++	++
Cerebral cortex	+/−	+++ (small)[a]

Distribution of spheroids and vacuoles in the CNS were assessed and graded as follows: +/−, very few; +, mild degree; ++, moderate degree; +++, marked degree.

[a]Vacuoles of small size were predominantly observed. Mice aged 95–103 weeks were examined.

not shown), confirming previous observations (Bao et al., 2004).

Neurodegeneration and shortened lifespan

Because we could not find any obvious abnormalities of *iPLA$_2\beta^{-/-}$* mice by the age of 1 year, except for reduced fertility in males, a substantial number of mice were kept alive to examine the effect on their lifespan and aging. Although at 40–50 weeks no difference of body weight between *iPLA$_2\beta^{-/-}$* mice and their littermates (supplemental Fig. 1*A*, available at www.jneurosci.org as supplemental material), *iPLA$_2\beta^{-/-}$* mice gradually lost weight and died earlier than their littermates (Fig. 3*A*,*B*). The log-rank test indicated there was a significant survival difference between *iPLA$_2\beta^{-/-}$* and *iPLA$_2\beta^{+/+}$* mice ($p < 0.02$), and between *iPLA$_2\beta^{-/-}$* and *iPLA$_2\beta^{+/-}$* mice ($p < 0.002$). The median lifespan of *iPLA$_2\beta^{-/-}$* mice was 90 weeks compared with 110–115 weeks for their littermates. By the age of 2 years, all of the *iPLA$_2\beta^{-/-}$* mice showed abnormal movement of their hindlimbs. When held by the tail, *iPLA$_2\beta^{-/-}$* mice moved their hindlimbs randomly in all directions or stopped moving with feet clasping, and a dangling posture being prominent (Fig. 4*Ad*,*Ae*). The mice seemed unable to use their hindlimbs to maintain their balance as they tried to raise their heads. In contrast, *iPLA$_2\beta^{+/+}$* mice extended their hindlimbs out from the trunk to maintain their balance (Fig. 4*Aa*,*Ab*), and could easily raise their heads. Moreover, *iPLA$_2\beta^{-/-}$* mice dragged their hindlimbs when walking and had an irregular stride (Fig. 4*B*). In contrast, *iPLA$_2\beta^{+/+}$* and *iPLA$_2\beta^{+/-}$* mice did not show any of these changes. When motor function was assessed by the hanging wire grip test, the mice were placed on a wire net that was turned upside down, and the time until the animal fell was recorded three times. Because body weight was predicted to affect the time until falling, the weight was plotted against time (Fig. 4*C*). All of the *iPLA$_2\beta^{-/-}$* mice showed impaired motor function in this test. The *iPLA$_2\beta^{-/-}$* mice also tended to adopt a hunched posture (Fig. 4*Af*), although x-ray radiograms did not reveal any obvious differences of bone structure or density (data not shown). After analysis of 2-year-old mice, the behavioral abnormalities of younger *iPLA$_2\beta^{-/-}$* mice (≤1 year old) were carefully monitored. Although *iPLA$_2\beta^{-/-}$* mice did not show obvious abnormalities in the footprint and tail suspension tests by the age of 55 weeks (supplemental Fig. 1*B*, available at www.jneurosci.org as supplemental material) (data not shown), the hanging wire grip test was definitely abnormal. Their time scores decreased gradually from the age of 30 weeks, and by the age of ~50 weeks all of the *iPLA$_2\beta^{-/-}$* mice showed very low time scores (Fig. 4*D*). These results indicate that the hanging wire grip test may be more sensitive for detecting impaired motor function in *iPLA$_2\beta^{-/-}$* mice. All together, these findings indicated that iPLA$_2\beta$ deficiency led to the onset of motor dysfunction and a shorter lifespan.

Neuropathological findings in *iPLA$_2\beta^{-/-}$* mice

The *iPLA$_2\beta^{-/-}$* mice were subjected to neuropathological studies and the changes observed at 2 years are summarized in Table 1. There were numerous spheroids or vacuoles in the axons and neuropil throughout the CNS (Fig. 5) and the peripheral nervous system (PNS) (Fig. 6), indicating the widespread degeneration of axons or synapses. These round or irregular spheroids were 3–90 μm in diameter. The larger spheroids frequently showed vacuolation, fissures, or rarefaction (Figs. 5*B*,*C*, 6*C*). As summarized in Table 1, the spheroids were most prominent in the tegmentum of the medulla (Fig. 5*B*), the lower pons, and the dorsal horns (Fig. 5*C*) of the entire spinal cord. In addition to the spheroids, vacuoles of various sizes (3–40 μm in diameter) were observed (Fig. 5*B*,*C*,*L*). Most of the larger vacuoles had a core (Fig. 5*B*,*C*). A single irregularly swollen axon that contained both spheroids and a vacuole was detected in a longitudinal section (Fig. 6*C*). The cerebral cortex contained numerous vacuoles, most of which were rather small (3–5 μm), and there were only a few spheroids (Fig. 5*L*). Younger *iPLA$_2\beta^{-/-}$* mice were also subjected to neuropathological examination and the following data were obtained. At 15 weeks, tiny vacuoles were frequently observed in the molecular layer of the cerebellum (Fig. 5*I*), which became atrophic at 2 years (Fig. 5*H*), and spheroids were also found in the dentate nucleus of the cerebellum (Fig. 5*J*). In other regions, vacuoles and spheroids were only rarely observed. At 32 weeks, some small vacuoles were found in the cerebral cortex, striatum, and hippocampus, and a number of spheroids and large vacuoles were observed in the tegmentum of the lower pons or medulla and in the spinal cord, as well as the cerebellum (data not shown). At 55 weeks, vacuoles or spheroids were distributed throughout the CNS (data not shown). PAS staining revealed many PAS-positive granules, mainly in the normal-looking axons of larger neurons such as anterior horn cells, where very few spheroids or vacuoles were found at 15 weeks (Fig. 5*E*). At 2 years, PAS-positive granules were also scattered in axons or the neuropil where spheroids were prominent (Fig. 5*F*). Both spheroids and vacuoles frequently contained PAS-positive granules (Fig. 5*C*). Although many of the spheroids were positive for PAS to some extent, spheroids were not stained by Berlin blue, which detects iron (data not shown). In *iPLA$_2\beta^{+/+}$* mice, a few spheroids and vacuoles were observed exclusively in the gracile nucleus and part of the cuneate nucleus (data not shown), which might have represented physiological neuroaxonal dystrophy occurring as part of the normal aging process.

Immunohistochemistry using an anti-phosphorylated neurofilament antibody (SMI31) revealed strong staining of some small spheroids, indicating that these structures originated from

balt6/zns-neusci/zns-neusci/zns00908/zns4528-08a | slaterl | S=7 | 2/18/08 | 15:16 | Art: 3323393 | Input-YY(v)

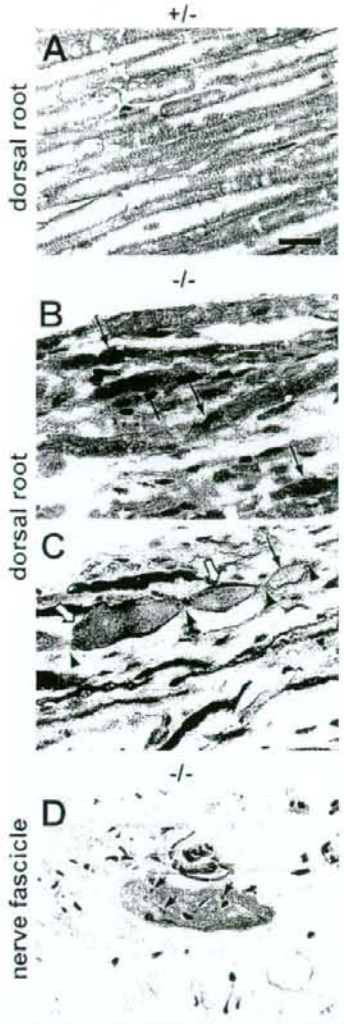

Figure 6. Pathological changes of the PNS. ***A–C***, Dorsal root of an *iPLA$_2\beta^{+/-}$* mouse (***A***) and an *iPLA$_2\beta^{-/-}$* mouse (***B***, ***C***) at 2 years. ***D***, Subcutaneous nerve fascicle of an *iPLA$_2\beta^{-/-}$* mouse at 2 years. ***A***, ***B***, and ***D*** are PAS stained. ***C***, Bielschowsky stain. Scale bar, 16 μm. ***A***, Axons of the *iPLA$_2\beta^{+/-}$* mouse are PAS negative, although the myelin sheath is weakly stained by PAS. ***B***, Swollen axons (arrows) are heterogeneously stained by PAS and contain strongly PAS-positive granules. ***C***, A single swollen axon contains both spheroids (open arrows) and a vacuole (arrow). The central parts of the spheroids (open arrows) are rarefied. Staining of the axonal structures (arrowheads) between the spheroids is weak. ***D***, PAS-positive granules can be seen in the nerve fascicle.

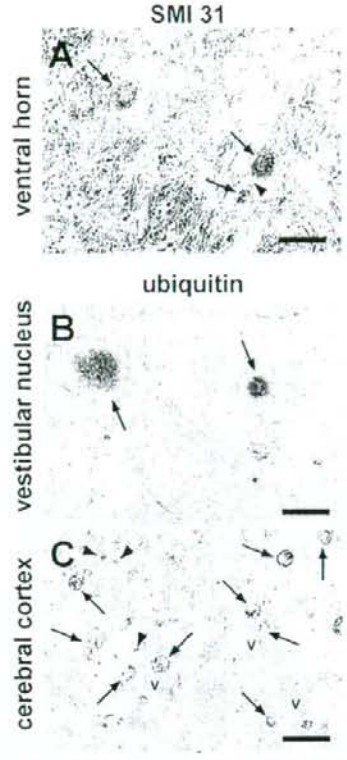

Figure 7. Immunohistochemical analysis of spheroids and vacuoles in *iPLA$_2\beta^{-/-}$* mice at 2 years. ***A***, Ventral horn was stained with anti-phosphorylated neurofilament H (SMI31). ***B***, ***C***, Vestibular nucleus (***B***) and cerebral cortex (***C***) were stained with anti-ubiquitin antibody. v, Vessels. Scale bars: ***A***, 20 μm; ***B***, 10 μm; ***C***, 16 μm. ***A***, Spheroids (arrows) are positive for SMI31, whereas the axonal portion between the spheroids (arrowhead) is negative. ***B***, Two spheroids (arrows) have positive cores. The other spheroid (asterisk) contains vacuoles that are weakly stained or unstained for ubiquitin. ***C***, Numerous vacuoles (arrows) and tiny circles (arrowheads) that are ubiquitin positive in the neuropil of the cerebral cortex.

F7 axons (Fig. 7*A*). Most of the large and irregular spheroids that contained narrow clefts or vacuoles were almost completely negative for this antibody, suggesting that severe degeneration had occurred. Some of the spheroids and vacuoles were also stained by anti-ubiquitin antibody, with the cores or fissures of the spheroids and the rims or inner contents of small vacuoles being stained to a varying extent (Fig. 7*B*,*C*). These findings indicate that some of the spheroids and vacuoles contained ubiquitinated proteins.

Morphological analysis of the sciatic nerve demonstrated that the total number of myelinated fibers (density by area) was significantly reduced in *iPLA$_2\beta^{-/-}$* mice (Table 2). The density of T2 myelinated fibers was similar (Table 2, supplemental Fig. 2*C*,*D*, available at www.jneurosci.org as supplemental material) in both groups, but the area of the nerve fascicles was significantly smaller in *iPLA$_2\beta^{-/-}$* mice (Table 2, supplemental Fig. 2*B*, available at www.jneurosci.org as supplemental material), indicating that the sciatic nerves of these mice had undergone atrophy because of neuronal degeneration.

Ultrastructural examination of *iPLA$_2\beta^{-/-}$* mice at 55 weeks showed that spheroids in the dorsal funiculus contained tubulovesicular structures, as well as vacuoles, vesicles, and amorphous matrix (Fig. 8). These tubulovesicular structures were also F8 found in the cerebral cortex (data not shown).

Discussion

We showed that iPLA$_2\beta$ deficiency in mice led to motor impairment, which was accompanied by the appearance of axonal swelling (spheroids) and vacuoles throughout the nervous system. Our results provide experimental evidence that iPLA$_2\beta$ plays a critical role in maintaining the structural and functional integrity

balt6/zns-neusci/zns-neusci/zns00908/zns4528-08a | slaterl | S=7 | 2/18/08 | 15:16 | Art: 3323393 | Input-YY(v)

Table 2. Morphological analysis of sciatic nerves between iPLA$_2\beta^{+/+}$ and iPLA$_2\beta^{-/-}$ mice

	Density of myelinated fibers (/mm^2)	Total area of nerve fascicles (mm^2)	Number of myelinated fibers (density × area)
$+/+$ ($n = 4$)	20156 ± 4007	0.189 ± 0.037	3735 ± 554
$-/-$ ($n = 7$)	22922 ± 1695	0.136 ± 0.117	3115 ± 234
		($p < 0.05$)	($p < 0.05$)

The number of myelinated fibers per unit area was counted in sciatic nerves. Mice aged 95–103 weeks old were examined. p values were calculated using the Student's t test.

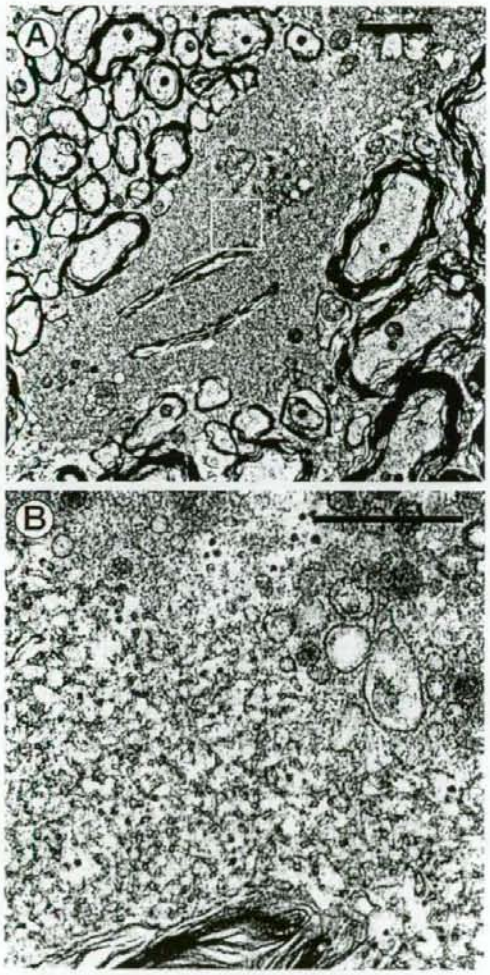

Figure 8. Electron microscopic features of spheroids. ***A***, ***B***, Dorsal faniculus of a *iPLA$_2\beta^{-/-}$* mouse at 56 weeks. ***B*** shows a higher magnification of the boxed region in ***A***. Tubulovesicular structures can be seen in the spheroid, as well as degenerated vesicles and vacuoles. Scale bars: ***A***, 2 μm; ***B***, 0.5 μm.

of axons or synapses, and that iPLA$_2\beta$ dysfunction leads to the occurrence of neuroaxonal dystrophy.

In this study, we found that *iPLA$_2\beta^{-/-}$* mice initially developed normally, but began to show significant motor dysfunction from the age of ~50 weeks (Fig. 4*D*), which progressed to ataxia and weakness by 2 years. These observations indicate that iPLA$_2\beta$ has an important role in maintaining the function of the nervous system, but not in nervous system development. INAD is caused by mutation of the *iPLA$_2\beta$* gene (Khateeb et al., 2006; Morgan et al., 2006) and patients develop the initial symptoms, including hypotonia, areflexia, or weakness < 2 years old. As the disease progresses, dementia, ataxia, blindness, and spasticity occur, and these patients die before puberty (Nardocci et al., 1999). Although some symptoms, such as weakness and ataxia, were common to INAD patients and *iPLA$_2\beta^{-/-}$* mice, the clinical course was different. In mice, the onset was late and disease progression was slow. The different clinical pictures could possibly be explained by species differences or compensation for iPLA$_2\beta$ deficiency by other PLA$_2$ isotypes (such as iPLA$_2\gamma$) in mice.

However, the neuropathological features seen in *iPLA$_2\beta^{-/-}$* mice were very similar to those found in patients with INAD. Neuroaxonal dystrophy in INAD and NBIA is characterized by a morphological change of axons in the CNS, which is the development of spheroids (Seitelberger, 1952). Numerous spheroids and vacuoles were distributed throughout the CNS in the *iPLA$_2\beta^{-/-}$* mice (Table 1), as is also observed in INAD. As has been reported for INAD (Gonatas et al., 1967), the spheroids were located in the axons and synapses of *iPLA$_2\beta^{-/-}$* mice (Figs. 5, 6). In addition, the cerebellum (which is one of the most susceptible regions in INAD) (Nardocci et al., 1999) seemed to be affected quite early among the CNS regions in *iPLA$_2\beta^{-/-}$* mice (Fig. 5*I*,*J*). Furthermore, examination of the sciatic nerves of *iPLA$_2\beta^{-/-}$* mice showed peripheral nerve degeneration (Table 2, supplemental Fig. 2, available at www.jneurosci.org as supplemental material), as also occurs in INAD (Duncan et al., 1970). Moreover, tubulovesicular structures, which are a characteristic finding in INAD patients (Gonatas et al., 1967), were detected in *iPLA$_2\beta^{-/-}$* mice by electron microscopy (Fig. 8). Because the pathological changes of the nervous system were almost identical, the *iPLA$_2\beta^{-/-}$* mouse seems to be an appropriate model for studying the detailed pathogenesis of neuroaxonal dystrophy in INAD.

AQ: 1

The mechanisms leading to the formation of spheroids and vacuoles in the absence of functional iPLA$_2\beta$ remain unclear, but these structures seem to arise from the degeneration of axons or synaptic terminals. Some of the large vacuoles presumably developed from the resorption of spheroids (Cowen and Olmstead, 1963) via a process involving ubiquitination (Fig. 7*B*). Because numerous PAS-positive granules appeared in the axons or neuropil by 15 weeks, which was before the spheroids and vacuoles formed (Fig. 5*E*), and because both spheroids and large vacuoles contained PAS-positive granules (Figs. 5*C*, 6*B*), these granules might be the key to elucidating the pathogenesis of neuroaxonal degeneration in *iPLA$_2\beta^{-/-}$* mice and INAD patients. Because PAS stains materials containing aldehydes as well as staining polysaccharides like glycogen, the PAS-positive material might represent accumulations of polysaccharides, aberrantly glycated proteins, or aldehyde products of lipid peroxides created by an increase of ROS in the iPLA$_2\beta$-deficient state.

iPLA$_2\beta$ is an important enzyme for maintaining phospholipid membranes through the processes of phospholipid turnover, remodeling, and repair (Ma and Turk, 2001). Therefore, iPLA$_2\beta$ deficiency may alter the phospholipid composition of cellular

and subcellular membranes, or may lead to failure to repair oxidative damage to membrane phospholipids, resulting in changes of membrane permeability, fluidity, or ion homeostasis. Why are the axons or presynaptic terminals, and not the cytoplasm, selectively affected in INAD patients and *iPLA$_2\beta^{-/-}$* mice? The tubulovesicular structures observed in both INAD patients and *iPLA$_2\beta^{-/-}$* mice (Fig. 8) are believed to result from degenerated ER or mitochondria. iPLA$_2\beta$ has been reported to exist in and protect mitochondria (Seleznev et al., 2006), as well as being abundant in neurites and axon terminals (Ong et al., 2005), so its absence would contribute to damage targeting mitochondria in axons and synaptic terminals, leading to degeneration of the axons and synaptic terminals.

Some individuals with NBIA, formerly known as Hallervorden-Spatz syndrome, have a mutation of the pantothenate kinase 2 (*PANK2*) gene (Zhou et al., 2001). The product of this gene is an enzyme localized to the mitochondria (Kotzbauer et al., 2005) and involved in the biosynthesis of coenzyme A (CoA), which has various roles that include acting as a carrier of free fatty acids. Oxidative damage or impaired fatty acid metabolism resulting from mitochondrial CoA deficiency is thought to be a possible cause of neurodegenerative changes (Johnson et al., 2004). The common mechanism of neuroaxonal dystrophy in iPLA$_2\beta$ deficiency and PANK2 deficiency may be mitochondrial dysfunction affecting the axons and/or axon terminals. Clarification of the pathogenesis of neuroaxonal dystrophy in *iPLA$_2\beta^{-/-}$* mice will hopefully lead to the development of treatments for INAD and other neurodegenerative disorders.

AQ: J

References

Balboa MA, Varela-Nieto I, Killermann Lucas K, Dennis EA (2002) Expression and function of phospholipase A(2) in brain. FEBS Lett 531:12–17.

Bao S, Miller DJ, Ma Z, Wohltmann M, Eng G, Ramanadham S, Moley K, Turk J (2004) Male mice that do not express group VIA phospholipase A2 produce spermatozoa with impaired motility and have greatly reduced fertility. J Biol Chem 279:38194–38200.

Cowen D, Olmstead EV (1963) Infantile neuroaxonal dystrophy. J Neuropathol Exp Neurol 22:175–236.

Duncan C, Strub R, McGarry P, Duncan D (1970) Peripheral nerve biopsy as an aid to diagnosis in infantile neuroaxonal dystrophy. Neurology 20:1024–1032.

Farooqui AA, Ong WY, Horrocks LA (2004) Biochemical aspects of neurodegeneration in human brain: involvement of neural membrane phospholipids and phospholipases A2. Neurochem Res 29:1961–1977.

Gonatas NK, Evangelista I, Walsh GO (1967) Axonic and synaptic changes in a case of psychomotor retardation: an electron microscopic study. J Neuropathol Exp Neurol 26:179–199.

Inoue N, Ikawa M, Isotani A, Okabe M (2005) The immunoglobulin superfamily protein Izumo is required for sperm to fuse with eggs. Nature 434:234–238.

Johnson MA, Kuo YM, Westaway SK, Parker SM, Ching KH, Gitschier J, Hayflick SJ (2004) Mitochondrial localization of human PANK2 and hypotheses of secondary iron accumulation in pantothenate kinase-associated neurodegeneration. Ann NY Acad Sci 1012:282–298.

Khateeb S, Flusser H, Ofir R, Shelef I, Narkis G, Vardi G, Shorer Z, Levy R, Galil A, Elbedour K, Birk OS (2006) PLA2G6 mutation underlies infantile neuroaxonal dystrophy. Am J Hum Genet 79:942–948.

Kotzbauer PT, Truax AC, Trojanowski JQ, Lee VM (2005) Altered neuronal mitochondrial coenzyme A synthesis in neurodegeneration with brain iron accumulation caused by abnormal processing, stability, and catalytic activity of mutant pantothenate kinase 2. J Neurosci 25:689–698.

Ma Z, Turk J (2001) The molecular biology of the group VIA Ca^{2+}-independent phospholipase A2. Prog Nucleic Acid Res Mol Biol 67:1–33.

Mancuso DJ, Jenkins CM, Gross RW (2000) The genomic organization, complete mRNA sequence, cloning, and expression of a novel human intracellular membrane-associated calcium-independent phospholipase A(2). J Biol Chem 275:9937–9945.

Matsuoka Y, Matsuoka Y, Shibata S, Ban T, Toratani N, Shigekawa M, Ishida H, Yoneda Y (2002) A chromodomain-containing nuclear protein, MRG15 is expressed as a novel type of dendritic mRNA in neurons. Neurosci Res 42:299–308.

Morgan NV, Westaway SK, Morton JE, Gregory A, Gissen P, Sonek S, Cangul H, Coryell J, Canham N, Nardocci N, Zorzi G, Pasha S, Rodriguez D, Desguerre I, Mubaidin A, Bertini E, Trembath RC, Simonati A, Schanen C, Johnson CA, et al. (2006) PLA2G6, encoding a phospholipase A(2), is mutated in neurodegenerative disorders with high brain iron. Nat Genet 38:752–754.

AQ: K

Nardocci N, Zorzi G, Farina L, Binelli S, Scaioli W, Ciano C, Verga L, Angelini L, Savoiardo M, Bugiani O (1999) Infantile neuroaxonal dystrophy: clinical spectrum and diagnostic criteria. Neurology 52:1472–1478.

Ong WY, Yeo IF, Ling SF, Farooqui AA (2005) Distribution of calcium-independent phospholipase A2 (iPLA 2) in monkey brain. J Neurocytol 34:447–458.

Seitelberger F (1952) Eine unbekannte Form von infantiler Lipoidspeicher-Krankheit des Gehirns. Proc 1st Int Congr Neuropathol 3:323–333.

Seleznev K, Zhao C, Zhang XH, Song K, Ma ZA (2006) Calcium-independent phospholipase A2 localizes in and protects mitochondria during apoptotic induction by staurosporine. J Biol Chem 281:22275–22288.

Shinzawa K, Tsujimoto Y (2003) PLA2 activity is required for nuclear shrinkage in caspase-independent cell death. J Cell Biol 163:1219–1230.

Six DA, Dennis EA (2000) The expanding superfamily of phospholipase A(2) enzymes: classification and characterization. Biochim Biophys Acta 1488:1–19.

Sumi H, Nagano S, Fujimura H, Kato S, Sakoda S (2006) Inverse correlation between the formation of mitochondria-derived vacuoles and Lewy-body-like hyaline inclusions in G93A superoxide-dismutase-transgenic mice. Acta Neuropathol (Berl) 112:52–63.

Tang J, Kriz RW, Wolfman N, Shaffer M, Seehra J, Jones SS (1997) A novel cytosolic calcium-independent phospholipase A2 contains eight ankyrin motifs. J Biol Chem 272:8567–8575.

Yang HC, Mosior M, Ni B, Dennis EA (1999) Regional distribution, ontogeny, purification, and characterization of the Ca^{2+}-independent phospholipase A2 from rat brain. J Neurochem 73:1278–1287.

Zhong Y, Takemoto M, Fukuda T, Hattori Y, Murakami F, Nakajima D, Nakayama M, Yamamoto N (2004) Identification of the genes that are expressed in the upper layers of the neocortex. Cereb Cortex 14:1144–1152.

Zhou B, Westaway SK, Levinson B, Johnson MA, Gitschier J, Hayflick SJ (2001) A novel pantothenate kinase gene (PANK2) is defective in Hallervorden-Spatz syndrome. Nat Genet 28:345–349.

Available online at www.sciencedirect.com
ScienceDirect
Journal of Nutritional Biochemistry xx (2007) xxx–xxx
Journal of Nutritional Biochemistry

Allicin inhibits cell growth and induces apoptosis through the mitochondrial pathway in HL60 and U937 cells

Talia Miron[a,*], Meir Wilchek[a], Ayala Sharp[b], Yoshihito Nakagawa[c], Makoto Naoi[c], Yoshinori Nozawa[c], Yukihiro Akao[c]

[a]Department of Biological Chemistry, Weizmann Institute of Science, Rehovot 76100, Israel
[b]Department of Biological Services, Weizmann Institute of Science, Rehovot 76100, Israel
[c]Gifu International Institute of Biotechnology, Kakamigahara, Gifu 504-0838, Japan

Received 22 April 2007; received in revised form 12 June 2007; accepted 20 June 2007

Abstract

In this article, the effects of allicin, a biological active compound of garlic, on HL60 and U937 cell lines were examined. Allicin induced growth inhibition and elicited apoptotic events such as blebbing, mitochondrial membrane depolarization, cytochrome *c* release into the cytosol, activation of caspase 9 and caspase 3 and DNA fragmentation. Pretreatment of HL60 cells with cyclosporine A, an inhibitor of the mitochondrial permeability transition pore (mPTP), inhibited allicin-treated cell death. HL60 cell survival after 1 h pretreatment with cyclosporine A, followed by 16 h in presence of allicin (5 μM) was ~80% compared to allicin treatment alone (~50%). Also *N*-acetyl cysteine, a reduced glutathione (GSH) precursor, prevented cell death. The effects of cyclosporine A and *N*-acetyl cysteine suggest the involvement of mPTP and intracellular GSH level in the cytotoxicity. Indeed, allicin depleted GSH in the cytosol and mitochondria, and buthionine sulfoximine, a specific inhibitor of GSH synthesis, significantly augmented allicin-induced apoptosis. In HL60 cells treated with allicin (5 μM, 30 min) the redox state for 2GSH/oxidized glutathione shifted from E_{GSH} −240 to −170 mV. The same shift was observed in U937 cells treated with allicin at a higher concentration for a longer period of incubation (20 μM, 2 h). The apoptotic events induced by various concentrations of allicin correlate to intracellular GSH levels in the two cell types tested (HL60: 3.7 nmol/10^6 cells; U937: 7.7 nmol/10^6 cells). The emerging mechanistic basis for the antiproliferative function of allicin, therefore, involves the activation of the mitochondrial apoptotic pathway by GSH depletion and by changes in the intracellular redox status.

Keywords: Allicin; Apoptosis; Garlic; GSH; HL60; U937

1. Introduction

Allicin, diallyl thiosulfinate, is the main biologically active compound derived from garlic. It is produced by the interaction of the enzyme alliinase (alliin lyase; EC 4.4.1.4) with its substrate alliin (*S*-allyl-L-cysteine sulfoxide) [1]. Since alliinase and alliin are enclosed in different compartments within the garlic clove cells, intact garlic cloves do not contain allicin. When the garlic clove is crushed, alliin and alliinase interact, to form allicin, pyruvic acid and ammonia (Scheme 1). Allicin became an object of interest due to its potential to confer a vast spectrum of health beneficial effects including: anti microbial, antifungal and antiparasitic [2], antihypertensive [3], cardioprotective [4–6], anti-inflammatory [7] and anticancer activities [2,8,9].

In vitro studies of allicin's effect on human mammary MCF-7 cancer cells revealed that its antiproliferative activity is accompanied by accumulation of cells in the regulatory checkpoints, G_0/G_1 and G_2/M, of the cell cycle [9]. Interestingly, also other ally sulfur compound cause similar effects [10]. Allicin was shown to induce apoptosis in gastric

Abbreviations: BSO, D,L-buthionine *S,R*-sulfoximine; CsA, Cyclosporin A; DTNB, 5,5′-dithiobis-(2-nitrobenzoic acid); GGCS, γ-Glutamyl-L-cysteine synthetase; GSH, Reduced glutathione; GSSA, *S*-allylmercaptoglutathione; GSSG, Oxidized glutathione; mPTP, Mitochondrial permeability transition pore; NAC, *N*-acetyl-L-cysteine; XTT, 2,3-Bis (2-methoxy-4-nitro-5-sulfophenyl)-2*H*-tetrazolium-5-carboxanilide sodium salt.

* Corresponding author. Tel.: +972 8 9343627; fax: +972 8 9468256.
E-mail address: talia.miron@weizmann.ac.il (T. Miron).

0955-2863/$ – see front matter © 2007 Published by Elsevier Inc.
doi:10.1016/j.jnutbio.2007.06.009

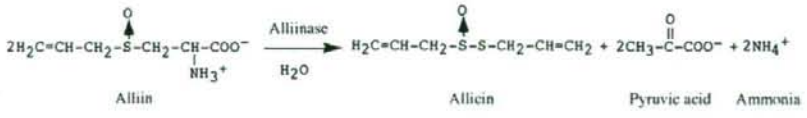

Scheme 1.

cancer SGC-7901 cells. The cause of apoptosis was related to decreased telomerase activity, an enzyme which allicin inhibits in a time- and dose- dependent manner [11]. Allicin induces apoptosis in human cervical cancer SiHa cells and mouse fibroblast-like L-929 cells, manifested through the appearance of characteristic apoptotic morphological changes in apoptotic bodies, through DNA fragmentation, and activation of caspases 8, 9 and 3 [12]. Allicin was also shown to induce apoptosis in human epithelial carcinoma through a caspase-independent pathway, mediated by the release of apoptotic-inducing factor (AIF) from mitochondria and protein kinase A (PKA) activation [13]. More results describing the effects of allicin or other garlic-derived products on various proteins participate in the apoptotic process have already been reported [14]. However, the mechanism underlying the induction of cell death by allicin has not been fully elucidated.

Apoptosis is an ordered cascade of events that culminates in cell death. Two main pathways of apoptosis have been characterized. The extrinsic pathway is initiated through ligand stimulation of the cell surface death receptors such as TNFR or CD95R. In this pathway, cell death is executed via a cascade of proteolytic events with the sequential activation of caspase 8 and caspase 3. The intrinsic pathway is triggered by mitochondrial stress caused by various factors such as DNA damage, oxidative stress and heat shock (reviewed [15]). This pathway is initiated through the release of signal factors from mitochondria as a consequence of mitochondrial membrane permeability transition. Such changes lead to translocation of pro- and antiapoptotic proteins across the mitochondrial membranes [16,17]. Among these proteins is cytochrome *c*, which is released from the mitochondria to the cytosol and participates with other molecules in the formation of a complex that activates caspase 9, which in turn activates caspase 3. The activation of these caspases leads to the final fragmentation of nuclear DNA, with the typical apoptotic morphological manifestations.

Allicin easily diffuses through cell membranes (diffusion coefficient 5×10^{-8} cm^2s^{-1}) [18] and exerts its biological effects by reacting with free thiols within the cell. In living cells, reduced glutathione (GSH) is the major free thiol participating in cellular redox reactions and mixed disulfide formation. GSH is therefore the main cellular target of allicin reaction (Scheme 2). Both allicin and its glutathione derivative, *S*-allylmercaptoglutathione (GSSA), can prevent the formation of free radicals. GSSA is similar in this preventive capacity to GSH, both being less effective in this antioxidant activity than allicin [19–21]. Allicin can scavenge the chain-carrying peroxyl radicals of the substrates by transferring its allylic hydrogen to the oxidized substrate. This renders it a stronger antioxidant than its derivatives [22].

Allicin is a short-lived compound, which rapidly reacts with free intracellular thiol groups [18,19,22]. It was found to disintegrate in the blood a few minutes after its administration, both in vitro in human blood [23] and in vivo in rats [24]. Therefore, the therapeutic effect of allicin administered orally may be restricted to targets that are close to the gastrointestinal tract. However, its main oxidation products, *S*-allylmercapto-glutathione and *S*-allylmercapto-cysteine, could exert their action in more remote sites within the body because they are more stable. The rapid disappearance of allicin can be exploited in tumor cells targeting. We previously showed that allicin kills tumor cells in vitro [25,26] and also in vivo if generated on their surface by conjugating alliinase to monoclonal antibodies directed to specific cell-surface receptors, such as ErbB2, overexpressed in breast and ovarian cancer [25]; CD20, a receptor expressed at high levels in human B chronic lymphocytic leukemia and other B-cell lymphomas [26].

The redox environment of a cell reflects the sum of the products of the reduction potential and the reducing capacity of the linked redox couples operating within the cell [27,28] Glutathione is considered to be the major thiol-disulfide redox buffer of cells [29]. The redox state of the 2GSH/oxidized glutathione (GSSG) redox couple depends on their molar ratio. Upon reacting with GSH, allicin causes a decrease in free GSH concentration and an increase in mixed-disulfide glutathione products, which leads to an increase in the reduction potential values. Allicin also reacts

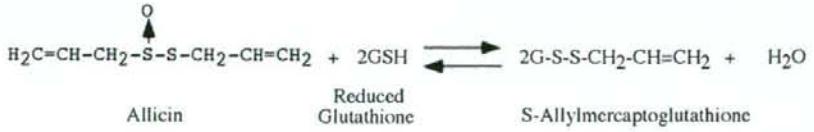

Scheme 2.